CrossMark

ORIGINAL PAPER

A novel approach to computational homogenization and its application to fully coupled two-scale thermomechanics

Robert Fleischhauer[1] · **Marko Božić**[1] · **Michael Kaliske**[1]

Abstract The paper introduces a novel approach to computational homogenization by bridging the scales from microscale to macroscale. Whenever the microstructure is in an equilibrium state, the macrostructure needs to be in equilibrium, too. The novel approach is based on the concept of representative volume elements, stating that an assemblage of representative elements should be able to resemble the macrostructure. The resulting key assumption is the continuity of the appropriate kinematic fields across both scales. This assumption motivates the following idea. In contrast to existing approaches, where mostly constitutive quantities are homogenized, the balance equations, that drive the considered field quantities, are homogenized. The approach is applied to the fully coupled partial differential equations of thermomechanics solved by the finite element (FE) method. A novel consistent finite homogenization element is given with respect to discretized residual formulations and linearization terms. The presented FE has no restrictions regarding the thermomechanical constitutive laws that are characterizing the microstructure. A first verification of the presented approach is carried out against semi-analytical and reference solutions within the range of one-dimensional small strain thermoelasticity. Further verification is obtained by a comparison to the classical FE^2 method and its different types of boundary conditions within a finite deformation setting of purely mechanical problems. Furthermore, the efficiency of the novel approach is investigated and compared. Finally, structural examples are shown in order to demonstrate the applicability of the presented homogenization framework in case of finite thermo-inelasticity at different length scales.

Notation and abbreviations

Symbols and operators

$\bigcup$	Assemble operator
$\vert$	Condition on the given set
D	Gateaux derivative
$\wedge$	Logical and
$\overline{\Box}$	Macroscopic quantity, e.g., $\overline{\boldsymbol{\sigma}}$
$\dot{\Box}$	Material time derivative
∂_x	Partial derivative with respect to x
∂_{xy}^2	Second order partial derivative with respect to x, y
div	Spatial divergence operator
grad	Spatial gradient operator
sym	Symmetry operator
d	Total derivative
$\Box^T$	Transposition operator
$\forall$	Universal quantifier

Thermomechanical quantities

θ	Absolute temperature
$\mathbf{K}$	Assembled stiffness matrix
$\boldsymbol{\sigma}$	Cauchy stress tensor
$\mathcal{B}_t$	Current configuration
$\boldsymbol{g}$	Current metric tensor

✉ Michael Kaliske
michael.kaliske@tu-dresden.de

1 Institute for Structural Analysis, Technische Universität Dresden, 01062 Dresden, Germany

Springer

$\boldsymbol{x}$	Current position vector
$\boldsymbol{F}$	Deformation gradient
J	Determinant of deformation gradient
$\boldsymbol{u}$	Displacement vector
w_{ext}	External power term
r	Internal heat source
w_{int}	Internal power term
$\boldsymbol{q}$	Spatial heat flux vector
q_n	Spatial heat flow
$\boldsymbol{t}$	Spatial surface traction
$\boldsymbol{d}$	Symmetric part of spatial velocity gradient
ϑ	Temperature change with respect to reference temperature
q_p	Thermal power
$\mathbf{R}$	Vector of residuals
$\mathbf{x}$	Vector of unknowns

Abbreviations

BVDH	Boundary value driven approach to computational homogenization
FE	Finite element
FEM	Finite element method
LDBC	Linear displacement boundary conditions
PDBC	Periodic displacement boundary conditions
PDE	Partial differential equation
RVE	Representative volume element
SST	Substructure
UTBC	Uniform traction boundary conditions

1 Introduction

The numerical analysis of the behavior of structures or sub-structures (SSTs) is often required in engineering tasks. Applied loads to be considered might be of mechanical and/or of thermal nature. The structural behavior is dependent on the mechanical and thermal properties of the materials as well as on their micro-, meso- and macroscopic composition. An interaction of these properties might be of importance for engineering analyzes. Especially, if large deformations combined with heat conduction or dissipative phenomena are present, heat generation and convection within or at the surface of the structure need to be considered. These effects are often due to the application of synthetic materials such as polymers. Additionally, polymers can be reinforced by, e.g., particles or fibers, in order to improve their strength or stiffness for specific purposes during their operating life. Macroscopic structures, such as, e.g., bearings or car bumpers, made of reinforced synthetic materials, are usually characterized by a microscopic length scale, due to the rein-

forcement. Thus, a length scale ratio between, e.g., 1 μm and 1 m is observed with respect to the heterogeneity of the structure. The length scale ratio usually leads to high computational effort if heterogeneous structures shall be resolved by the numerical discretization. This effort arises from the spatial discretization in combination with multiphysics of the underlying problem which is a main aspect of consideration of this investigation. Thus, efficient homogenization methods, which are applicable to fully coupled thermo-inelasticity are required. The paper at hand presents an improved efficiency compared to classical FE[2] frameworks. Furthermore, no limitations are existing in the presented approach regarding the constitutive thermomechanical laws with respect to homogenizing heterogeneous structural responses at different length scales, which is an unpublished aspect so far.

In recent years, remarkable progress in the field of computational homogenization in structural engineering has been made, see, e.g., [1–3] and references therein for a review. Various approaches have been proposed in literature in order to derive and to obtain homogenization methods for purely mechanical problems. The window or superframe method, introduced in [4], computes effective properties of a microstructural sample in terms of statistical representativeness by embedding the microstructure into a superframe of a homogeneous material and therewith achieves faster convergence of the macroscopic effective properties. The authors assume the equations of linear elasticity as basis for their computational analysis of composite systems. The optimality of the convergence of the window method is investigated and its basis is depicted in [5], where furthermore a comparison with classical homogenization method results is carried out. A numerical plate testing procedure is presented in [6], where especially composite plates with an intrinsic in-plane periodicity of the heterogeneous microstructure is considered. This approach introduces shell elements at the macroscale and volume elements at the micro-level as well as a consistent coupling between the different degrees of freedom at the different length scales. The authors perform a verification of their method with respect to plate and laminate theories.

An adaptive formulation based on a material map from micro- to macroscale has been developed in [7]. This kind of database methodology is used in order to determine the effective macroscopic behavior of orthotropic nonlinear elasticity. In [8,9], effective properties of linear elastic composite microstructures are derived by averaging them over the microstructure. The homogenized quantities are further used for the macroscopic stress analysis within an finite element method (FEM) framework. Other approaches, see, e.g., [10–17] use a microscopic fine scale fluctuation field in order to determine the microstructural deformation state depending on the mechanical boundary conditions. It is based on certain assumptions for the boundary data of such a microstructure. Once the mechanical microstructure equi-

librium is computed, stresses and stiffness for the related material point within the macrostructure are determined. Higher order approximations for the scale-bridging deformation gradient are introduced and used in [18–20] among others. In [21], the computation of the macroscopic tangent is investigated taking the microscopic fluctuation field into account and a procedure for determining the stiffness from a stress controlled testing method at the microscale is developed.

Different from the assumption of fully separated scales, the authors of [22] consider the case of strongly coupled FE meshes at different length scales. The strong coupling of the displacement field across the scales is carried out by placing certain boundary nodes of the microscale at positions within the macrostructure, where macro-nodes are existing. This methodology preserves uniqueness of the displacements at certain points, but in between these unique points, microscale-displacements are interpolated linearly. The approach presented in [22] is investigated with respect to inelastic heterogeneous microstructures. Similarly, in [23] embedding of micro elements into a macrostructure with respect to a multiscale FE solution is described. The authors construct numerical base functions, assuming, e.g., linear boundary conditions or periodic boundary conditions of the microstructure, in order to relate the displacements of both scales. This approach is derived in the context of small strain elasto-plasticity at the microstructure.

Multiphysical computational homogenization methods, e.g., considering thermomechanics, are still developing. In [24], a staggered algorithm, which determines the macroscopic stresses and heat fluxes from the averaging over the microscale within a nested FEM procedure, is introduced. The authors of [25] provide a homogenization method in case of continuum thermomechanics, which yields macroscopic stresses and heat flux, based on the Irving–Kirkwood procedure. Therefore, they introduce a weighting function, which relates the quantities, such as mass, linear momentum and energy of the microscopic scale to the macroscopic scale. The authors derive from their approach Hill–Mandel-like conditions for stress and deformation as well as for heat flux and temperature gradient. Porous solids with microscale heat transfer are considered in [26]. The authors derive a method for thermo-mechanical analysis at two length scales, based on asymptotic expansion of the governing evolution equations of the displacements and temperatures with respect to small strain thermo-elasticity.

A model reduction technique combined with a homogenization approach is used in [27] in order to solve thermal and electrical conduction problems efficiently and precisely based on periodic microstructures as well as orthogonal decomposition methods. Macroscopic quantities are identified in [28] by averaging of the appropriate microscopic quantities separately over the microstructure in terms of

finite thermoelasticity. In [29], steady-state microscopic thermo-dynamic wave propagation equations are derived from higher-order methods in homogenization by means of an asymptotic multiscale homogenization approach. Furthermore, using the asymptotic expansion for thermomechanical homogenization, in [30] two uncoupled cells at the microscale are introduced and obtained, one for the mechanical field and one for the thermal field. The publication [31] utilizes computational homogenization in combination with statistical tests to compute the effective thermal conductivity of hardened cement paste under consideration of the variation of water content in the micropores. In [32], a hydro–thermo–chemo-mechanical coupling regarding homogenization is presented, where a combination of the classical linear displacement boundary conditions (LDBCs) and the window method is applied. Using this strategy, effective quantities are computed and associated with statistical analysis in order to predict and investigate problems with alkali-silica reactions of concrete.

Besides multiphysical homogenization strategies, multiscale approaches towards cracks and delamination phenomena are under investigation in recent years. In [33], a non-local theory is developed for damage of brittle composites by applying an asymptotic expansion in order to obtain overall macroscopic properties. The computation of effective macroscopic properties due to certain mesoscopic structures under consideration of damage and fracture processes for concrete is proposed in [34]. Recently in [35], a multiscale cohesive approach is developed for coupling the microscale damage evolution with the resulting macroscopic properties. A scale bridging method for cohesive interfaces at the macroscale and a representative volume element (RVE) at the microscale are proposed in [36], where the macroscopic properties are computed via homogenization. A contribution using a homogenization technique for predicting crack propagation and coalescence of cracks at the micro- and macroscale in an extended FE framework is given in [37]. Concluding, efficiency and generality regarding multiphysics of computational homogenization approaches need to be further developed and improved.

This contribution introduces the boundary value driven approach to computational homogenization (BVDH), which is applied to fully coupled thermomechanics. The different length scales are consistently coupled and considered within BVDH as well as a fully coupled thermomechanical framework without any requirements on the constitutive descriptions regarding thermo-inelasticity and therewith, dissipative material behavior is provided. BVDH is based on a continuous setting over all length scales of the considered field quantities, here the temperature and the displacements in an macroscopic equilibrium state. Therewith, the key idea is the homogenization of the thermomechanical balance equations, namely the linear momentum and the thermal power.

Fig. 1 Sketch of a heterogeneous macrostructure ($\overline{\mathcal{B}}_t$), its partition into possible substructures (SSTs) and one specific SST ($\mathcal{B}_{t^{\mathrm{SST}}}$)
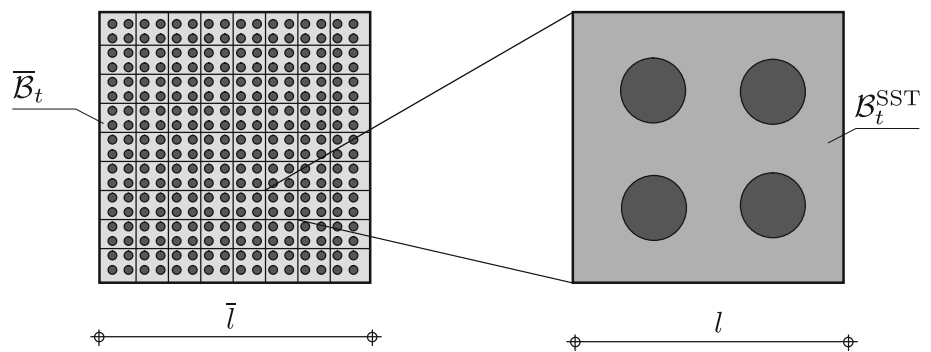
In combination with the kinematic assumptions and their treatment as well as scale bridging in terms of BVDH, these features are not existing so far in computational homogenization frameworks. Moreover, comparing computation times of BVDH solutions to existing methods, BVDH turns out to be numerically more efficient. This comparison is made by applying BVDH to purely mechanical problems, since no comparable method is existing with respect to fully coupled thermo-inelasticity at finite deformations of heterogeneous solids.

The paper is structured as follows. First, the theoretical setting of BVDH is given, where kinematics and thermomechanics at different length scales are introduced. Second, the continuous BVDH formulation is linearized and developed to be implemented into an FEM framework. Third, an algorithmic treatment for the FE implementation is developed and given. In order to verify BVDH, numerical verification examples follow, starting with a comparison of BVDH, a semi-analytical solution and a reference solution for one-dimensional thermoelasticity at small strains. A further verification of BVDH is carried out for three-dimensional mechanical examples at finite deformations, comparing the reliability and efficiency of BVDH to FE^2 frameworks. Additionally, a comparative study with respect to the length scale ratio δ and h-convergence behavior is presented. The paper closes with an application example of an inelastic and thermomechanical structural investigation, where the predicted numerical results are compared to experimental data.

2 A boundary value driven approach to computational homogenization

The following sections introduce and investigate theoretical as well as algorithmic aspects of BVDH. The first section deals with the developed theory, which is based on the underlying one-scale heterogeneous problem of a solid body in the current configuration, while the second section contains the algorithmic aspects of the proposed computational homogenization method.

2.1 Theoretical setting

Consider a heterogeneous body, e.g., a fiber reinforced polymer, as schematically depicted in Fig. 1. The macrostructure $\overline{\mathcal{B}}_t$ has a current volume $\overline{v} = \int \mathrm{d}\overline{v}$, based on the length scale $\overline{l}$ and can be divided into certain SSTs $\mathcal{B}_t^{\mathrm{SST}}$, having a current volume $v = \int \mathrm{d}v$ with a length scale l, such that

$$\overline{\mathcal{B}}_t = \bigcup_{\mathrm{SST}=1}^{N} \mathcal{B}_t^{\mathrm{SST}}, \tag{1}$$

$$\overline{v} = \int_{\overline{\mathcal{B}}_t} \mathrm{d}\overline{v} = \sum_{SST=1}^{N} \left[\int_{\mathcal{B}_t^{\mathrm{SST}}} \mathrm{d}v \right], \tag{2}$$

hold. Following the concepts of RVEs, one of the SSTs might fulfill the requirements of being chosen as an RVE. BVDH is not restricted to considering periodic RVEs as long as the RVEs are representative for the thermomechanical properties of the microstructure of the considered heterogeneous solid. The RVE has a current volume v and a typical length scale l. Evaluating

$$\delta = \frac{v}{\overline{v}}, \tag{3}$$

leads to the observation $1 \gg \delta > 0$, since any chosen RVE has a non-zero volume. For any load, that is applied to the macrostructure, a numerical FEM solution, based on a discretization across all length scales, can be achieved. Obviously, this one-scale discretization can lead to a very large number of degrees of freedom, as soon as δ is very small. Discretizing the heterogeneous body with FEs and solving the one-scale problem with a standard Newton-type FEM leads to a structural response, which can be used as a reference solution for numerical results obtained by a homogenization approach.

2.1.1 Kinematics and isoparametrical relations at different length scales

Since macroscopic displacements $\overline{u}(\overline{x}, t)$ and macroscopic temperature changes $\overline{\vartheta}(\overline{x}, t) = \overline{\theta}(\overline{x}, t) - \overline{\theta}_0$ are the

unknowns of interest for obtaining structural responses on the macroscopic length scale, the following kinematical definitions are introduced.

First, a homogenization domain decomposition of the macrostructure $\overline{\mathcal{B}}_t$ denotes the basis for macroscopic solutions with BVDH. Figure 2 shows schematically the BVDH domain decomposition, which is based on the assumptions

$$\overline{\mathcal{B}}_t = \bigcup_{\overline{E}=1}^{\overline{N}} \overline{\mathcal{B}}_{t_{\overline{E}}}, \tag{4}$$

$$\overline{\mathcal{B}}_{t_{\overline{E}}} := \left\{ \text{SST}_1, \ldots, \text{SST}_{N_{\text{SST}}} \mid \text{SST} = \mathcal{B}_{t_{\text{RVE}}} \right\}, \tag{5}$$

$$\mathcal{B}_{t_{\text{RVE}}} = \bigcup_{E=1}^{N} \mathcal{B}_{t_E}.. \tag{6}$$

Equation (4) states nothing more than a standard spatial discretization of a macrostructure $\overline{\mathcal{B}}_t$, having a current volume $\overline{v}$, into macroscopic FEs $\overline{\mathcal{B}}_{t_{\overline{E}}}$, having a current element volume $\overline{v}^{\overline{E}}$. The procedure leads to a discretization of the displacement and temperature field ($\{\overline{u}, \overline{\vartheta}\}$) within $\overline{\mathcal{B}}_t$ such that both fields can be evaluated at the introduced nodal points $\overline{x}^{\overline{E}}$. Equation (5) states that the physical properties of every of these macroscopic FEs $\overline{\mathcal{B}}_{t_{\overline{E}}}$ are sufficiently described by a set of SSTs, that fulfill the conditions of being an RVE. Every RVE $\mathcal{B}_{t_{\text{RVE}}}$ has a current volume $v = \int \mathrm{d}v$. Essential for the homogenization domain decomposition and for Eq. (5) is the condition

$$\overline{v} = \sum_{\overline{E}=1}^{\overline{N}} \int_{\overline{\mathcal{B}}_{t_{\overline{E}}}} \mathrm{d}\overline{v} = \sum_{\overline{E}=1}^{\overline{N}} \int_{\overline{\mathcal{B}}_{t_{\overline{E}}}} \left(\frac{1}{v} \int_{\mathcal{B}_{t_{\text{RVE}}}} \mathrm{d}v \right) \mathrm{d}\overline{v}. \tag{7}$$

After a spatial discretization of the macrostructure into macroscopic FEs ($\overline{\mathcal{B}}_{t_{\overline{E}}}$), the assignment of the RVEs ($\mathcal{B}_{t_{\text{RVE}}}$) to their positions within the macroscopic FEs has to be carried out. Using a numerical integration scheme, e.g., Gaussian quadrature, for determining the RVE volumes (v) and the macroscopic volume ($\overline{v}$), spatial integration points are required. Equation (7) can only hold if the volume average over the microscopic volume is related to macroscopic integration points. This requirement implies the position for every single RVE as well as the total amount N_{SST} of RVEs per macroscopic element during a numerical FEM solution, which makes use of a numerical integration scheme. Equation (6) can be seen as being a standard FE decomposition. A further assumption for the discretized kinematical relations of BVDH is denoted by the fact, that every point of an RVE in an equilibrium state can be mapped on its position within the macrostructure according to

$$\overline{x} = x \quad \forall \left(x \in \mathcal{B}_{t_{\text{RVE}}} \wedge x \in \partial \mathcal{B}_{t_{\text{RVE}}} \right). \tag{8}$$

This principal assumption is motivated by the underlying one-scale discretization, compare Fig. 1 and Eq. (1), where obviously the boundary data of $\overline{\mathcal{B}}_t$ drives the boundary of the SSTs. All unknown field quantities, evaluated at the boundaries of the SSTs, reassemble the macroscopic unknown field quantities. Hence, the identities

$$\overline{u}(\overline{x}, t) = u(x, t) \quad \forall \left(x \in \mathcal{B}_{t_{\text{RVE}}} \wedge x \in \partial \mathcal{B}_{t_{\text{RVE}}} \right), \tag{9}$$

$$\overline{\vartheta}(\overline{x}, t) = \vartheta(x, t) \quad \forall \left(x \in \mathcal{B}_{t_{\text{RVE}}} \wedge x \in \partial \mathcal{B}_{t_{\text{RVE}}} \right), \tag{10}$$

are introduced. This homogenization domain decomposition and its assumptions are motivated and strengthened by the fact, that a macrostructure, which is driven by certain boundary conditions, such as displacements or temperature and which can be divided into SSTs, is in a thermomechanical equilibrium state as soon as every SST is in an equilibrium state.

This implies, that every one-scale equilibrium denotes the reference and benchmark state for any homogenized structure. Now, the test functions for the two unknown fields are introduced according to

$$\delta u(x) := \left\{ \delta u(x) \in \mathcal{B}_{t_{\text{RVE}}} \mid \delta u(x) = \delta \overline{u}(\overline{x}) \, \forall x \in \partial \mathcal{B}_{t_{\text{RVE}u}} \right\}, \tag{11}$$

$$\delta \vartheta(x) := \left\{ \delta \theta(x) \in \mathcal{B}_{t_{\text{RVE}}} \mid \delta \theta(x) = \delta \overline{\vartheta}(\overline{x}) \, \forall x \in \partial \mathcal{B}_{t_{\text{RVE}\vartheta}} \right\}. \tag{12}$$

Equations (11) and (12) relate the microscopic test functions to the macroscopic test functions $\delta \overline{u}(\overline{x})$ and $\delta \overline{\vartheta}(\overline{x})$ at the boundaries of $\mathcal{B}_{t_{\text{RVE}}}$. The boundary of an RVE $\mathcal{B}_{t_{\text{RVE}}}$ is denoted by

$$\partial \mathcal{B}_{t_{\text{RVE}}} := \left\{ \partial \mathcal{B}_{t_{\text{RVE}u}}, \partial \mathcal{B}_{t_{\text{RVE}\vartheta}} \right\}, \tag{13}$$

where only displacements and temperature are prescribed at $\partial \mathcal{B}_{t_{\text{RVE}}}$. The test function definitions

$$\delta \overline{u}(\overline{x}) := \left\{ \delta \overline{u}(\overline{x}) \in \overline{\mathcal{B}}_t \mid \delta \overline{u} = \mathbf{0} \, \forall \overline{x} \in \partial \overline{\mathcal{B}}_{t_u} \right\}, \tag{14}$$

$$\delta \overline{\vartheta}(\overline{x}) := \left\{ \delta \overline{\vartheta}(\overline{x}) \in \overline{\mathcal{B}}_t \mid \delta \overline{\vartheta} = 0 \, \forall \overline{x} \in \partial \overline{\mathcal{B}}_{t_\theta} \right\}, \tag{15}$$

at the macroscopic scale ensure their continuity

$$\delta \overline{u}(\overline{x}) = \delta u(x) \quad \forall x, \tag{16}$$

$$\delta \overline{\vartheta}(\overline{x}) = \delta \vartheta(x) \quad \forall x, \tag{17}$$

over the whole macroscopic domain $\overline{\mathcal{B}}_t$, including all RVEs. Equations (16) and (17) are in accordance with the assumptions of Eqs. (9) and (10). Additionally, the interpolation functions $N(\xi)$ for the microscopic unknown fields and related test function, within the domain $\mathcal{B}_{t_E}$ of
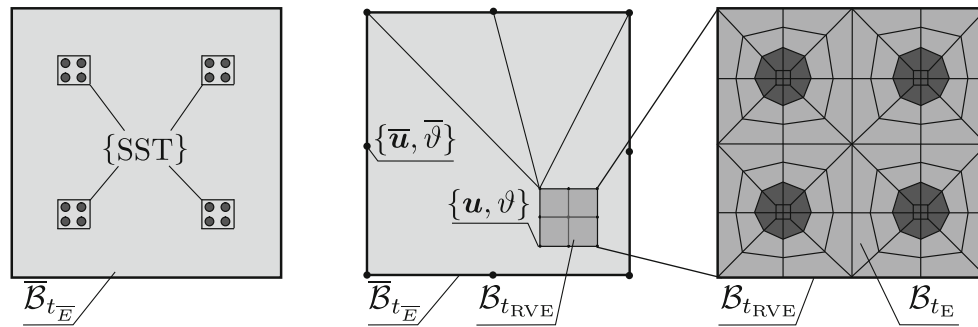
Fig. 2 Sketch of a macroscopic BVDH finite element $\overline{\mathcal{B}}_{t_{\overline{E}}}$ containing a set of substructures (SSTs), the isoparametric relations of the discretized unknown macro fields ($\{\overline{\boldsymbol{u}}, \overline{\vartheta}\}$) and unknown micro fields

($\{\boldsymbol{u}, \vartheta\}$) between $\overline{\mathcal{B}}_{t_{\overline{E}}}$ and a $\mathcal{B}_{t_{RVE}}$ boundary node, as well as a chosen RVE ($\mathcal{B}_{t_{RVE}}$) with a schematic discretization into microscopic FEs $\mathcal{B}_{t_E}$

$\mathcal{B}_{t_{RVE}}$, are introduced. Therefore, the isoparametric relations of the unknown and test function fields read, e.g., $\boldsymbol{u}(\boldsymbol{x}, t) = N(\boldsymbol{\xi})^I \boldsymbol{u}^I$ and $\vartheta(\boldsymbol{x}, t) = N(\boldsymbol{\xi})^I \vartheta^I$, where $I = 1, \ldots, I^E$ denotes the index for a single node of $\mathcal{B}_{t_E}$, having I^E nodes. The appropriate gradients are given by, e.g., $\mathrm{grad}\boldsymbol{u}(\boldsymbol{x}, t) = \frac{\partial}{\partial \boldsymbol{x}} N(\boldsymbol{\xi})^I \boldsymbol{u}^I$ and $\mathrm{grad}\vartheta(\boldsymbol{x}, t) = \frac{\partial}{\partial \boldsymbol{x}} N(\boldsymbol{\xi})^I \vartheta^I$, where $\frac{\partial}{\partial \boldsymbol{x}_i} N(\boldsymbol{\xi})^I = \boldsymbol{B}_i^I$ is abbreviated in the following. The shape or interpolation functions for the domain $\overline{\mathcal{B}}_{t_{\overline{E}}}$ are introduced according to, e.g., $\overline{\boldsymbol{u}}(\overline{\boldsymbol{x}}, t) = \overline{N}(\overline{\boldsymbol{\xi}})^I \overline{\boldsymbol{u}}^I$ and $\overline{\vartheta}(\overline{\boldsymbol{x}}, t) = \overline{N}(\overline{\boldsymbol{\xi}})^I \overline{\vartheta}^I$. Making use of the isoparametric relations within the macrostructure and using the identities of Eqs. (16) and (17), obviously every unknown quantity, e.g., temperature, of the boundary nodal points can be interpolated from the driving macroscale boundary conditions at the macroscopic FE nodes $\overline{\boldsymbol{x}}^E$ and can be used as boundary conditions for the equilibrium of $\mathcal{B}_{t_{RVE}}$ according to

$$\boldsymbol{u}(\boldsymbol{x}, t) = \overline{N}(\overline{\boldsymbol{\xi}})^I \overline{\boldsymbol{u}}^I \quad \forall \boldsymbol{x} \in \partial \mathcal{B}_{t_{RVE}}, \tag{18}$$

$$\vartheta(\boldsymbol{x}, t) = \overline{N}(\overline{\boldsymbol{\xi}})^I \overline{\vartheta}^I \quad \forall \boldsymbol{x} \in \partial \mathcal{B}_{t_{RVE}}. \tag{19}$$

Equations (18) and (19) are essential for prescribing the boundary data of the RVE. Figure 2 illustrates schematically this procedure.

2.1.2 Thermomechanical equilibrium at different length scales

In order to obtain a mechanical or thermomechanical FEM solution for a macrostructure as exemplarily depicted in Fig. 1, the balance of linear momentum and the transient heat conduction equation are dealt with by Galerkin's method. The starting point for obtaining the thermomechanical equilibrium state is the equilibrium at the microscale, reading in its local form

$$\rho \ddot{\boldsymbol{u}} = \rho \boldsymbol{b} + \mathrm{div}(\boldsymbol{\sigma}), \tag{20}$$

$$\rho c \dot{\theta} = -\mathrm{div}(\boldsymbol{q}) + \rho r + \rho w_{\mathrm{ext}} - \rho w_{\mathrm{int}}, \tag{21}$$

with respect to the current configuration of the RVE. The external and internal power terms are given by

$$\rho w_{\mathrm{ext}} = \rho \left[\theta 2 \partial_{\boldsymbol{g}\theta}^2 \psi \right] : \boldsymbol{d}, \tag{22}$$

$$\rho w_{\mathrm{int}} = \rho \left[\partial_{\mathcal{I}} \psi - \theta \partial_{\mathcal{I}\theta}^2 \psi \right] : \dot{\mathcal{I}}, \tag{23}$$

introducing the Helmholtz free energy ψ, the current metric $\boldsymbol{g}$, the symmetric part of the spatial velocity gradient $\boldsymbol{d}$ as well as any set of internal variables $\mathcal{I}$. The heat flux $\boldsymbol{q}$ is assumed to follow Fourier's law for isotropic conductive material behavior according to

$$\boldsymbol{q} = -\frac{k}{J} \mathrm{grad}\vartheta, \tag{24}$$

but is not restricted to it. The macroscopic partial differential equations (PDEs) for deriving the equilibrium read

$$\overline{\rho \ddot{\boldsymbol{u}}} = \overline{\rho \boldsymbol{b}} + \overline{\mathrm{div}(\boldsymbol{\sigma})}, \tag{25}$$

$$\overline{\rho c \dot{\theta}} = -\overline{\mathrm{div}(\boldsymbol{q})} + \overline{\rho r} + \overline{\rho w_{\mathrm{ext}}} - \overline{\rho w_{\mathrm{int}}}, \tag{26}$$

where $\overline{(\bullet)}$ denotes in the following a quantity defined at the macroscopic scale. Using Galerkin's method, the next step is the multiplication of Eqs. (20), (21), (25) and (26) with the appropriate test function and their integration over the domains $\mathcal{B}_{t_{RVE}}$ and $\overline{\mathcal{B}}_t$, respectively, reading for the RVE

$$0 = \int_{\mathcal{B}_{t_{RVE}}} \delta \boldsymbol{u} \cdot [\mathrm{div}(\boldsymbol{\sigma}) + \rho \boldsymbol{b} - \rho \ddot{\boldsymbol{u}}] \mathrm{d}v, \tag{27}$$

$$0 = \int_{\mathcal{B}_{t_{RVE}}} \delta \vartheta \left[\rho c \dot{\theta} + \mathrm{div}(\boldsymbol{q}) - \rho r \right.$$
$$\left. - \rho w_{\mathrm{ext}} + \rho w_{\mathrm{int}} \right] \mathrm{d}v. \tag{28}$$

Considering a one-scale solution, the discretization effort is tremendous as soon as the scale ratio δ is very small. In the context of computational homogenization, one can reduce it by considering a small number of RVEs within the macroscopic domain $\overline{\mathcal{B}}_t$ as long as Eq. (7) is fulfilled. The corresponding macroscopic global form is given by

$$\int_{\overline{\mathcal{B}}_t} \delta\overline{u} \cdot [\overline{\rho b} + \overline{\mathrm{div}(\sigma)} - \overline{\rho\ddot{u}}]\mathrm{d}\overline{v} = 0, \tag{29}$$

$$\int_{\overline{\mathcal{B}}_t} \delta\overline{\vartheta} \left[\overline{c\dot{\theta}} + \overline{\mathrm{div}(q)} - \overline{\rho r} - \overline{\rho w}_{\mathrm{ext}} + \overline{\rho w}_{\mathrm{int}}\right]\mathrm{d}\overline{v} = 0. \tag{30}$$

Recasting the divergences in Eq. (27) to Eq. (30)

$$\delta u \cdot \mathrm{div}(\sigma) = \mathrm{div}(\sigma\,\delta u) - \mathrm{grad}(\delta u):\sigma, \tag{31}$$

$$\delta\overline{u} \cdot \overline{\mathrm{div}(\sigma)} = \overline{\mathrm{div}(\sigma\,\delta u)} - \overline{\mathrm{grad}(\delta u):\sigma}, \tag{32}$$

$$\delta\vartheta\,\mathrm{div}(q) = \mathrm{div}(\delta\vartheta\,q) - q \cdot \mathrm{grad}(\delta\vartheta), \tag{33}$$

$$\delta\overline{\vartheta}\,\overline{\mathrm{div}(q)} = \overline{\mathrm{div}(\delta\vartheta\,q)} - \overline{q \cdot \mathrm{grad}(\delta\vartheta)}, \tag{34}$$

and applying the Gauss theorem leads to the continuous formulation, which will be numerically solved by the FEM and which reads for both scales

$$\int_{\partial\mathcal{B}_{t\mathrm{RVE}t}} \delta u \cdot t\,\mathrm{d}a = \int_{\mathcal{B}_{t\mathrm{RVE}}} \mathrm{grad}\delta u:\sigma \\ - \delta u \cdot (\rho b - \rho\ddot{u})\mathrm{d}v, \tag{35}$$

$$-\int_{\partial\mathcal{B}_{t\mathrm{RVE}q}} \delta\vartheta\, q_n\,\mathrm{d}a = \int_{\mathcal{B}_{t\mathrm{RVE}}} \delta\vartheta\left(\rho c\dot{\theta} - \rho r\right. \\ \left. -\rho w_{\mathrm{ext}} + \rho w_{\mathrm{int}}\right) \\ - \mathrm{grad}(\delta\vartheta) \cdot q\,\mathrm{d}v, \tag{36}$$

$$\int_{\partial\overline{\mathcal{B}}_{t\overline{t}}} \delta\overline{u} \cdot \overline{t}\,\mathrm{d}\overline{a} = \int_{\overline{\mathcal{B}}_t} \overline{\mathrm{grad}\delta u:\sigma} \\ - \delta\overline{u} \cdot (\overline{\rho b} - \overline{\rho\ddot{u}})\mathrm{d}\overline{v}, \tag{37}$$

$$-\int_{\partial\overline{\mathcal{B}}_{t\overline{q}}} \delta\overline{\vartheta}\,\overline{q}_n\,\mathrm{d}\overline{a} = \int_{\overline{\mathcal{B}}_t} \delta\overline{\vartheta}\left(\overline{\rho c\dot{\theta}} - \overline{\rho r}\right. \\ \left. -\overline{\rho w}_{\mathrm{ext}} + \overline{\rho w}_{\mathrm{int}}\right) \\ - \overline{\mathrm{grad}(\delta\vartheta) \cdot q}\,\mathrm{d}\overline{v}. \tag{38}$$

Considering that the RVE is driven by the thermomechanical unknowns as the boundary data, see Eq. (13), the right hand side of Eqs. (35) and (36) are assumed to be zero. Recalling the volume average of homogenization

$$\overline{(\bullet)} = \frac{1}{v}\int_v (\bullet)\mathrm{d}v, \tag{39}$$

where a macroscopic quantity $\overline{(\bullet)}$ is computed by the integration of the appropriate microscopic quantity $(\bullet)$ over a specific volume v, Eq. (39) is applied to Eqs. (35) and (36). Therewith, the microthermomechanical equilibrium state of a specific RVE is related to a macroscopic material point. The application of the volume average to the weak forms of the RVE equilibrium conditions needs to ensure, that the average of a product of two functions is equal to the product of the averages of two functions. Considering, e.g., an arbitrary function $f(x)$ defined within the volume of an RVE, the relations

$$\frac{1}{v}\int_v \delta u(x)f(x)\mathrm{d}v = \overline{\delta u(x)f(x)} = \delta\overline{u}(\overline{x})\overline{f}(\overline{x}), \tag{40}$$

hold as long as the properties of the test functions ensure this. Among other possibilities, e.g., any constant test function $(\delta u(x) := \{\delta u(x) = \mathrm{const.}\,\forall x \in v \land \delta u(x) = \mathbf{0}\,\forall x \in \partial v\})$ within the integration domain ensures that the average of the product of that constant with an arbitrary function is equal to the product of the averages of both functions at a frozen time t. The use of Eq. (39) in combination with a computational homogenization scheme allows now to relate an RVE to an integration point of a macroscopic FE $\overline{\mathcal{B}}_{t_{\overline{E}}}$. This assumption reduces the discretization effort over the domain $\overline{\mathcal{B}}_{t_{\overline{E}}}$ drastically, compared to a one-scale solution, which can be clearly seen from the comparison of Figs. 1 and 2. Therewith, the homogenized version of Eq. (35), connected to a material point within $\overline{\mathcal{B}}_t$, is given by

$$\overline{\mathrm{grad}\delta u:\sigma} - \delta\overline{u} \cdot (\overline{\rho b} - \overline{\rho\ddot{u}}) \\ = \frac{1}{v}\int_{\mathcal{B}_{t\mathrm{RVE}}} \mathrm{grad}\delta u:\sigma - \delta u \cdot (\rho b - \rho\ddot{u})\mathrm{d}v, \tag{41}$$

and the homogenized version of Eq. (36) reads

$$\delta\overline{\vartheta}\left(\overline{\rho c\dot{\theta}} - \overline{\rho r} - \overline{\rho w}_{\mathrm{ext}} + \overline{\rho w}_{\mathrm{int}}\right) - \overline{\mathrm{grad}(\delta\vartheta) \cdot q} \\ = \frac{1}{v}\int_{\mathcal{B}_{t\mathrm{RVE}}} \delta\vartheta\left(\rho c\dot{\theta} - \rho r - \rho w_{\mathrm{ext}} + \rho w_{\mathrm{int}}\right) \\ - \mathrm{grad}(\delta\vartheta) \cdot q\,\mathrm{d}v. \tag{42}$$

The identification of Eq. (41) as the internal contribution to Eq. (37) as well as Eq. (42) as the internal contribution to Eq. (38) provides the scale bridging from microscale to macroscale.

The introduced way of relating both scales is new compared to classical and existing methods of computational homogenization. Intrinsically, no restrictions on constitutive descriptions are necessary regarding BVDH, since the balance laws are homogenized in an equilibrium state. The generality of considering the complete set of thermomechanical balance equations removes the necessity of introducing additional assumptions for homogenizing specific constitutive quantities, such as stresses or heat fluxes. The Hill condition, see [38], and its resulting conditions for the boundary data of the microstructure lead to these additional assumptions in classical approaches. Consequently, they have to be determined for every single quantity to be homogenized.

The weak form of the macroscopic thermomechanical equilibrium state reads in a continuous formulation

$$
\int\limits_{\partial \overline{\mathcal{B}}_{t_{\overline{t}}}} \delta \overline{\boldsymbol{u}} \cdot \overline{\boldsymbol{t}} \mathrm{d}\overline{a}
$$
$$
= \int\limits_{\overline{\mathcal{B}}_t} \frac{1}{v} \int\limits_{\mathcal{B}_{t_{\mathrm{RVE}}}} \mathrm{grad}\delta \boldsymbol{u} : \boldsymbol{\sigma} - \delta \boldsymbol{u} \cdot (\rho \boldsymbol{b} - \rho \ddot{\boldsymbol{u}}) \mathrm{d}v \mathrm{d}\overline{v}, \tag{43}
$$
$$
- \int\limits_{\partial \overline{\mathcal{B}}_{t_{\overline{q}}}} \delta \overline{\vartheta} \overline{q}_n \mathrm{d}\overline{a}
$$
$$
= \int\limits_{\overline{\mathcal{B}}_t} \frac{1}{v} \int\limits_{\mathcal{B}_{t_{\mathrm{RVE}}}} \delta \vartheta \left(\rho c \dot{\theta} - \rho r - \rho w_{\mathrm{ext}} + \rho w_{\mathrm{int}} \right)
$$
$$
- \mathrm{grad}(\delta \vartheta) \cdot \boldsymbol{q} \mathrm{d}v \mathrm{d}\overline{v}. \tag{44}
$$

Since quasi-static solutions are considered in this study, inertia and body force terms of Eq. (43) are neglected in the following. The spatially discretized microscopic nodal reactions are obtained from Eqs. (43) and (44)

$$
\boldsymbol{R}^{EI}_{\mathrm{mec}_i} = \int\limits_{\mathcal{B}_{t_E}} \boldsymbol{B}^I_j \boldsymbol{\sigma}_{ij} \mathrm{d}v, \tag{45}
$$

$$
\boldsymbol{R}^{EI}_{\mathrm{the}} = \int\limits_{\mathcal{B}_{t_E}} N^I \left(\rho c \dot{\theta} - \rho r - \rho w_{\mathrm{ext}} + \rho w_{\mathrm{int}} \right)
$$
$$
- \boldsymbol{B}^I_i \boldsymbol{q}_i \mathrm{d}v. \tag{46}
$$

Knowing that the macroscopic solution state is dependent on the microscale equilibrium, which is obtained by an FEM solution for every RVE, no inner nodal reactions are present, meaning

$$
\boldsymbol{R}^{EI}_{\mathrm{mec}_i} = 0 \quad \forall \left\{ I \in E \mid I \notin \partial \mathcal{B}_{t_{\mathrm{RVE}_{\boldsymbol{u}}}} \right\}, \tag{47}
$$

$$
\boldsymbol{R}^{EI}_{\mathrm{the}} = 0 \quad \forall \left\{ I \in E \mid I \notin \partial \mathcal{B}_{t_{\mathrm{RVE}_{\vartheta}}} \right\}, \tag{48}
$$

where implicitly a distinction between the inner nodes $\boldsymbol{x}_a \notin \partial \mathcal{B}_{t_{\mathrm{RVE}}}$ and the outer nodes $\boldsymbol{x}_b \in \partial \mathcal{B}_{t_{\mathrm{RVE}}}$ of the RVE is made. The boundary nodes $\boldsymbol{x}_b$ are driven by the nodal values of the surrounding macroscopic element domain $\overline{\mathcal{B}}_{t_{\overline{E}}}$ according to Eqs. (18) and (19). Considering Eq. (47), Eq. (43) can be recast into

$$
0 = \bigcup_{\overline{E}=1}^{\overline{N}} \int\limits_{\overline{\mathcal{B}}_{t_{\overline{E}}}} \frac{1}{v} \bigcup_{E=1}^{N} \delta \boldsymbol{u}^I_i \boldsymbol{R}^{EI}_{\mathrm{mec}_i} \mathrm{d}\overline{v}
$$
$$
- \bigcup_{\overline{E}=1}^{\overline{N}} \delta \overline{\boldsymbol{u}}^I_i \int\limits_{\partial \overline{\mathcal{B}}_{t_{\overline{Et}}}} \overline{N}(\overline{\boldsymbol{\xi}})^I \overline{t}_i \mathrm{d}\overline{a} \quad \forall \delta \boldsymbol{u}^I_i \in \partial \mathcal{B}_{t_{\mathrm{RVE}_{\boldsymbol{u}}}}. \tag{49}
$$

Similarly, Eq. (44) reads

$$
0 = \bigcup_{\overline{E}=1}^{\overline{N}} \int\limits_{\overline{\mathcal{B}}_{t_{\overline{E}}}} \frac{1}{v} \bigcup_{E=1}^{N} \delta \vartheta^I \boldsymbol{R}^{EI}_{\mathrm{the}} \mathrm{d}\overline{v}
$$
$$
+ \bigcup_{\overline{E}=1}^{\overline{N}} \delta \overline{\vartheta}^I \int\limits_{\partial \overline{\mathcal{B}}_{t_{\overline{Eq}}}} \overline{N}(\overline{\boldsymbol{\xi}})^I \overline{q}_n \mathrm{d}\overline{a} \quad \forall \delta \vartheta^I \in \partial \mathcal{B}_{t_{\mathrm{RVE}_{\vartheta}}}, \tag{50}
$$

under consideration of Eq. (48). Making use of the relations introduced in Eqs. (16), (17), (47), (48), (18), (19) and denoting $\overline{\boldsymbol{\xi}}_b := \overline{\boldsymbol{\xi}}(\boldsymbol{x}) \forall \boldsymbol{x} \in \partial \mathcal{B}_{t_{\mathrm{RVE}}}$, a further recasting of the macroscopic thermomechanical equilibrium state leads

$$
0 = \bigcup_{\overline{E}=1}^{\overline{N}} \delta \overline{\boldsymbol{u}}^I_i \int\limits_{\overline{\mathcal{B}}_{t_{\overline{E}}}} \frac{1}{v} \overline{N} \left(\overline{\boldsymbol{\xi}}_b \right)^I \bigcup_{E=1}^{N} \boldsymbol{R}^E_{\mathrm{mec}_i} \mathrm{d}\overline{v}
$$
$$
- \bigcup_{\overline{E}=1}^{\overline{N}} \delta \overline{\boldsymbol{u}}^I_i \int\limits_{\partial \overline{\mathcal{B}}_{t_{\overline{Et}}}} \overline{N}(\overline{\boldsymbol{\xi}})^I \overline{t}_i \mathrm{d}\overline{a}, \tag{51}
$$

$$
0 = \bigcup_{\overline{E}=1}^{\overline{N}} \delta \overline{\vartheta}^I \int\limits_{\overline{\mathcal{B}}_{t_{\overline{E}}}} \frac{1}{v} \overline{N} \left(\overline{\boldsymbol{\xi}}_b \right)^I \bigcup_{E=1}^{N} \boldsymbol{R}^E_{\mathrm{the}} \mathrm{d}\overline{v}
$$
$$
+ \bigcup_{\overline{E}=1}^{\overline{N}} \delta \overline{\vartheta}^I \int\limits_{\partial \overline{\mathcal{B}}_{t_{\overline{Eq}}}} \overline{N}(\overline{\boldsymbol{\xi}})^I \overline{q}_n \mathrm{d}\overline{a}. \tag{52}
$$

Within Eqs. (51) and (52), the identities of Eqs. (18) and (19) are used as well as the BVDH domain decomposition of Eqs. (4)–(6). A macroscopic BVDH FE residual can now be expressed for a macroscopic node $\overline{I}$ by

$$
\delta \overline{u}_i^I \overline{R}_{\mathrm{mec}_i}^I = \delta \overline{u}_i^I \int\limits_{\overline{\mathcal{B}}_{t_{\overline{E}}}} \frac{1}{v} \overline{N} \left(\overline{\xi}_b \right)^{\overline{I}} \bigcup_{E=1}^{N} R_{\mathrm{mec}_i}^E \, \mathrm{d}\overline{v}
$$
$$
- \int\limits_{\partial \overline{\mathcal{B}}_{t_{\overline{Et}}}} \overline{N}(\overline{\xi})^{\overline{I}} \overline{t}_i \, \mathrm{d}\overline{a}, \tag{53}
$$

for the mechanical field and by

$$
\delta \overline{\vartheta}^I \overline{R}_{\mathrm{the}}^I = \delta \overline{\vartheta}^I \int\limits_{\overline{\mathcal{B}}_{t_{\overline{E}}}} \frac{1}{v} \overline{N} \left(\overline{\xi}_b \right)^{\overline{I}} \bigcup_{E=1}^{N} R_{\mathrm{the}}^E \, \mathrm{d}\overline{v}
$$
$$
+ \int\limits_{\partial \overline{\mathcal{B}}_{t_{\overline{E\overline{q}}}}} \overline{N}(\overline{\xi})^{\overline{I}} \overline{q}_n \, \mathrm{d}\overline{a}, \tag{54}
$$

for the thermal field. The whole macroscopic domain $\overline{\mathcal{B}}_t$ can now be assembled from Eqs. (53) and (54) by use of Eq. (4). $\overline{R}_{\mathrm{mec}_i}^I$ and $\overline{R}_{\mathrm{the}}^I$ can be recast into

$$
\overline{R}_{\mathrm{mec}_i}^I = \int\limits_{\overline{\mathcal{B}}_{t_{\overline{E}}}} \frac{1}{v} \overline{N} \left(\overline{\xi}_b \right)^{\overline{I}} R_{\mathrm{mec}_i}^b \, \mathrm{d}\overline{v} - \int\limits_{\partial \overline{\mathcal{B}}_{t_{\overline{Et}}}} \overline{N}(\overline{\xi})^{\overline{I}} \overline{t}_i \, \mathrm{d}\overline{a}, \tag{55}
$$
$$
\overline{R}_{\mathrm{the}}^I = \int\limits_{\overline{\mathcal{B}}_{t_{\overline{E}}}} \frac{1}{v} \overline{N} \left(\overline{\xi}_b \right)^{\overline{I}} R_{\mathrm{the}}^b \, \mathrm{d}\overline{v} + \int\limits_{\partial \overline{\mathcal{B}}_{t_{\overline{E\overline{q}}}}} \overline{N}(\overline{\xi})^{\overline{I}} \overline{q}_n \, \mathrm{d}\overline{a}, \tag{56}
$$

since Eqs. (47) and (48) hold and the RVE domain is divided into inner and boundary nodes. What remains is the linearization and the discretization of the macroscopic thermomechanical equilibrium state, Eqs. (43) and (44), in order to achieve a fully coupled Newton-type FE solution.

2.1.3 Linearized thermomechanical equilibrium at different length scales

A consistent FE implementation, which enables a solution that rapidly converges to a thermomechanical equilibrium for Eqs. (49) and (50), requires a linearization of both equations for the macroscopic displacements and temperature changes. Having a look at the RVE FEM solutions, which are implied by Eqs. (55) and (56) and defining

$$
\mathbf{x} := \bigcup_{E=1}^{N} \begin{bmatrix} \boldsymbol{u}(\boldsymbol{x}, t)_a^I \ \forall \boldsymbol{x} \notin \partial \mathcal{B}_{t_{\mathrm{RVE}}} \\ \vartheta(\boldsymbol{x}, t)_a^I \ \forall \boldsymbol{x} \notin \partial \mathcal{B}_{t_{\mathrm{RVE}}} \\ \boldsymbol{u}(\boldsymbol{x}, t)_b^I \ \forall \boldsymbol{x} \in \partial \mathcal{B}_{t_{\mathrm{RVE}}} \\ \vartheta(\boldsymbol{x}, t)_b^I \ \forall \boldsymbol{x} \in \partial \mathcal{B}_{t_{\mathrm{RVE}}} \end{bmatrix} = \begin{bmatrix} \mathbf{x}_a \\ \mathbf{x}_b \end{bmatrix}, \tag{57}
$$

as well as

$$
\mathbf{R} := \bigcup_{E=1}^{N} \begin{bmatrix} \boldsymbol{R}^E(\boldsymbol{x}, t)_{\mathrm{mec}}^a \ \forall \boldsymbol{x} \notin \partial \mathcal{B}_{t_{\mathrm{RVE}}} \\ \boldsymbol{R}^E(\boldsymbol{x}, t)_{\mathrm{the}}^a \ \forall \boldsymbol{x} \notin \partial \mathcal{B}_{t_{\mathrm{RVE}}} \\ \boldsymbol{R}^E(\boldsymbol{x}, t)_{\mathrm{mec}}^b \ \forall \boldsymbol{x} \in \partial \mathcal{B}_{t_{\mathrm{RVE}}} \\ \boldsymbol{R}^E(\boldsymbol{x}, t)_{\mathrm{the}}^b \ \forall \boldsymbol{x} \in \partial \mathcal{B}_{t_{\mathrm{RVE}}} \end{bmatrix} = \begin{bmatrix} \mathbf{R}_a \\ \mathbf{R}_b \end{bmatrix}, \tag{58}
$$

the first step is recalling the definition of the microscopic thermomechanical RVE residual (under negligence of inertia and body force terms) as

$$
R_{\mathrm{mec}} = \int\limits_{\mathcal{B}_{t_{\mathrm{RVE}}}} \mathrm{grad} \delta \boldsymbol{u} : \boldsymbol{\sigma} \, \mathrm{d}v, \tag{59}
$$

$$
R_{\mathrm{the}} = \int\limits_{\mathcal{B}_{t_{\mathrm{RVE}}}} \delta \vartheta \left(\rho c \dot{\theta} - \rho r - \rho w_{\mathrm{ext}} + \rho w_{\mathrm{int}} \right)
$$
$$
- \mathrm{grad}(\delta \vartheta) \cdot \boldsymbol{q} \, \mathrm{d}v. \tag{60}
$$

This enables to follow the methodology of linearization for quasi-static analysis. First, a discretization of Eq. (59) is carried out, reading

$$
R_{\mathrm{mec}} = \bigcup_{E=1}^{N} \delta \boldsymbol{u}_k^I \int\limits_{\mathcal{B}_{t_E}} \boldsymbol{B}_l^I \sigma_{kl} \, \mathrm{d}v, \tag{61}
$$

as well as of Eq. (60), which can be expressed as

$$
R_{\mathrm{the}} = \bigcup_{E=1}^{N} \delta \vartheta^I \int\limits_{\mathcal{B}_{t_E}} N^I \left[\rho c \dot{\theta} - \rho r - \rho w_{\mathrm{ext}} + \rho w_{\mathrm{int}} \right]
$$
$$
- \boldsymbol{B}_k^I \boldsymbol{q}_k \, \mathrm{d}v. \tag{62}
$$

A linearization of Eq. (59) reads

$$
\mathrm{D}R_{\mathrm{mec}} = \int\limits_{\mathcal{B}_{t_{\mathrm{RVE}}}} \mathrm{grad} \delta \boldsymbol{u} : \left[\mathrm{grad}(\Delta \boldsymbol{u}) \boldsymbol{\sigma} \right.
$$
$$
\left. + \mathbb{C} : \mathrm{sym}(\mathrm{grad}(\Delta \boldsymbol{u})) - (\partial_\theta \boldsymbol{\sigma}) \Delta \theta \right] \mathrm{d}v. \tag{63}
$$

Neglecting any heat source inside the volume, the linearization term of Eq. (60) can be expressed as

$$
\mathrm{D}R_{\mathrm{the}} = \int\limits_{\mathcal{B}_{t_{\mathrm{RVE}}}} \delta \vartheta \left(\rho c \partial_\theta \dot{\theta} \Delta \vartheta \right.
$$
$$
- \partial_{\boldsymbol{u}} \rho w_{\mathrm{ext}} \cdot \Delta \boldsymbol{u} - \partial_\theta \rho w_{\mathrm{ext}} \Delta \vartheta
$$
$$
+ \partial_{\boldsymbol{u}} \rho w_{\mathrm{int}} \cdot \Delta \boldsymbol{u} + \partial_\theta \rho w_{\mathrm{int}} \Delta \vartheta \big)
$$
$$
- \mathrm{grad}(\delta \vartheta) \cdot \left[2 \mathrm{sym}(\mathrm{grad}(\Delta \boldsymbol{u}) \boldsymbol{q} \right.
$$
$$
\left. + \left(\frac{k}{J} \right) \mathrm{grad} \Delta \vartheta \right] \mathrm{d}v. \tag{64}
$$

The discretized form of Eq. (63) reads

$$
\begin{aligned}
\mathrm{D}R_{\mathrm{mec}} = \bigcup_{E=1}^{N} \delta \boldsymbol{u}_k^I & \left[\int_{\mathcal{B}_{t_E}} \boldsymbol{B}_i^I \boldsymbol{\sigma}_{ji} \boldsymbol{B}_j^J \delta_{km} \right. \\
& \left. + \boldsymbol{B}_i^I \mathbb{C}_{kimj} \boldsymbol{B}_j^J \mathrm{d}v \right] \Delta \boldsymbol{u}_m^J \\
& + \bigcup_{E=1}^{N} \delta \boldsymbol{u}_k^I \left[\int_{\mathcal{B}_{t_E}} \boldsymbol{B}_i^I \partial_\theta \boldsymbol{\sigma}_{ki} \boldsymbol{N}^J \mathrm{d}v \right] \Delta \vartheta^J,
\end{aligned}
\tag{65}
$$

and Eq. (64) can be discretized as

$$
\begin{aligned}
\mathrm{D}R_{\mathrm{the}} = \bigcup_{E=1}^{N} \delta \vartheta^I & \left[\int_{\mathcal{B}_{t_E}} \boldsymbol{B}_k^I \boldsymbol{q}_i \boldsymbol{B}_i^J + \boldsymbol{B}_i^I \boldsymbol{q}_k \boldsymbol{B}_i^J \right. \\
& - \boldsymbol{N}^I \left[(\partial_{\boldsymbol{g}_{ki}} \partial_\theta \boldsymbol{\sigma}_{mn} + \partial_{\boldsymbol{g}_{ik}} \partial_\theta \boldsymbol{\sigma}_{mn}) \colon \boldsymbol{d}_{mn} \boldsymbol{B}_i^J \right. \\
& \left. + \theta (\partial_\theta \boldsymbol{\sigma})_{ki} \boldsymbol{B}_i^J \frac{1}{\Delta t} + \theta (\partial_\theta \boldsymbol{\sigma})_{ji} \boldsymbol{l}_{kj} \boldsymbol{B}_i^J \right] \\
& \left. + \boldsymbol{N}^I \rho \left(\partial_{\boldsymbol{g}_{ki}} w_{\mathrm{int}} + \partial_{\boldsymbol{g}_{ik}} w_{\mathrm{int}} \right) \boldsymbol{B}_i^J \mathrm{d}v \right] \Delta \boldsymbol{u}_k^J \\
& + \bigcup_{E=1}^{N} \delta \vartheta^I \left[\int_{\mathcal{B}_{t_E}} \boldsymbol{N}^I \rho c \frac{1}{\Delta t} \boldsymbol{N}^J + \boldsymbol{B}_i^I (k/J) \boldsymbol{B}_i^J \right. \\
& - \boldsymbol{N}^I \rho w_{\mathrm{ext}} \boldsymbol{N}^J \\
& \left. + \boldsymbol{N}^I \rho w_{\mathrm{int}} \boldsymbol{N}^J \mathrm{d}v \right] \Delta \vartheta^J.
\end{aligned}
\tag{66}
$$

Equation (65) contains the mechanical part of the element stiffness as well as a coupling between the mechanical and the thermal field and can be rewritten as

$$
\mathrm{D}R_{\mathrm{mec}} = \bigcup_{E=1}^{N} \delta \boldsymbol{u}_k^I \left[\boldsymbol{K}_{\boldsymbol{uu}_{km}}^{EIJ} \right] \Delta \boldsymbol{u}_m^J
$$
$$
+ \bigcup_{E=1}^{N} \delta \boldsymbol{u}_k^I \left[\boldsymbol{K}_{\boldsymbol{u}\vartheta_k}^{EIJ} \right] \Delta \vartheta^J.
\tag{67}
$$

Equivalently, Eq. (66) contains the thermal part of the element stiffness as well as a coupling between the thermal and the mechanical field and can be given as

$$
\mathrm{D}R_{\mathrm{the}} = \bigcup_{E=1}^{N} \delta \vartheta^I \left[\boldsymbol{K}_{\vartheta \boldsymbol{u}_k}^{EIJ} \right] \Delta \boldsymbol{u}_k^J
$$
$$
+ \bigcup_{E=1}^{N} \delta \vartheta^I \left[\boldsymbol{K}_{\vartheta \vartheta}^{EIJ} \right] \Delta \vartheta^J.
\tag{68}
$$

Therewith, the microscopic element stiffness

$$
\boldsymbol{K}^{EIJ} = \begin{bmatrix} \boldsymbol{K}_{\boldsymbol{uu}}^{EIJ} & \boldsymbol{K}_{\boldsymbol{u}\vartheta}^{EIJ} \\ \boldsymbol{K}_{\vartheta \boldsymbol{u}}^{EIJ} & \boldsymbol{K}_{\vartheta \vartheta}^{EIJ} \end{bmatrix},
\tag{69}
$$

can be defined according to the order of nodes and degrees of freedom. Neglecting the inertia terms in Eq. (59) and considering a vector of nodal values for the test function fields $\delta \boldsymbol{u}$ and $\delta \vartheta$

$$
\delta \mathbf{x} := \bigcup_{E=1}^{N} \begin{bmatrix} \delta \boldsymbol{u}^I \\ \delta \vartheta^I \end{bmatrix},
\tag{70}
$$

and a vector of nodal values for the increments of the unknown fields

$$
\Delta \mathbf{x} := \bigcup_{E=1}^{N} \begin{bmatrix} \Delta \boldsymbol{u}^I \\ \Delta \vartheta^I \end{bmatrix}.
\tag{71}
$$

Equations (61), (62), (65) and (66) can now be formulated as

$$
\delta \mathbf{x}^T [\partial_{\mathbf{x}} \mathbf{R}] \Delta \mathbf{x} + \delta \mathbf{x}^T [\mathbf{R}] = 0,
\tag{72}
$$

where $[\partial_{\mathbf{x}} \mathbf{R}] =: \mathbf{K}$ is defined as the assembled RVE stiffness matrix reading

$$
\mathbf{K} = \bigcup_{E=1}^{N} \left[\boldsymbol{K}^E \right],
\tag{73}
$$

see Eq. (69). Furthermore, the assembled RVE residual vector, $[\mathbf{R}]$, compare Eq. (58), is used. For any admissible test function field, the solution of the microscopic thermomechanical equilibrium state for a quasi static and iterative FE solution can now be obtained by solving

$$
\mathbf{K} \Delta \mathbf{x} + \mathbf{R} = \mathbf{0},
\tag{74}
$$

in a typical time increment $\Delta t = t_{n+1} - t_n$. Considering the RVE partition into inner and boundary nodes, compare Eqs. (57) and (58), a similar decomposition can be carried out for

$$
\begin{aligned}
\mathbf{K} &= \begin{bmatrix} \partial_{\boldsymbol{u}_a} \boldsymbol{R}_{\mathrm{mec}}^a & \partial_{\vartheta_a} \boldsymbol{R}_{\mathrm{mec}}^a & \partial_{\boldsymbol{u}_b} \boldsymbol{R}_{\mathrm{mec}}^a & \partial_{\vartheta_b} \boldsymbol{R}_{\mathrm{mec}}^a \\ \partial_{\boldsymbol{u}_a} \boldsymbol{R}_{\mathrm{the}}^a & \partial_{\vartheta_a} \boldsymbol{R}_{\mathrm{the}}^a & \partial_{\boldsymbol{u}_b} \boldsymbol{R}_{\mathrm{the}}^a & \partial_{\vartheta_b} \boldsymbol{R}_{\mathrm{the}}^a \\ \partial_{\boldsymbol{u}_a} \boldsymbol{R}_{\mathrm{mec}}^b & \partial_{\vartheta_a} \boldsymbol{R}_{\mathrm{mec}}^b & \partial_{\boldsymbol{u}_b} \boldsymbol{R}_{\mathrm{mec}}^b & \partial_{\vartheta_b} \boldsymbol{R}_{\mathrm{mec}}^b \\ \partial_{\boldsymbol{u}_a} \boldsymbol{R}_{\mathrm{the}}^b & \partial_{\vartheta_a} \boldsymbol{R}_{\mathrm{the}}^b & \partial_{\boldsymbol{u}_b} \boldsymbol{R}_{\mathrm{the}}^b & \partial_{\vartheta_b} \boldsymbol{R}_{\mathrm{the}}^b \end{bmatrix} \\
&= \begin{bmatrix} \mathbf{K}_{aa} & \mathbf{K}_{ab} \\ \mathbf{K}_{ba} & \mathbf{K}_{bb} \end{bmatrix}.
\end{aligned}
\tag{75}
$$

The consistent linearization of Eqs. (55) and (56) is based on the assemblage of

$$
\overline{\mathbf{N}}_b^I := \left[\overline{N} \left(\bar{\boldsymbol{\xi}}_b \right)^I \right],
\tag{76}
$$

as well as on

$$\overline{\mathbf{R}}_{\overline{I}}^{\overline{E}} := \begin{bmatrix} \overline{\boldsymbol{R}}_{\mathrm{mec}}^{\overline{I}} \\ \overline{\boldsymbol{R}}_{\mathrm{the}}^{\overline{I}} \end{bmatrix}, \tag{77}$$

and

$$\overline{\mathbf{x}}_{\overline{I}}^{\overline{E}} := \begin{bmatrix} \overline{\boldsymbol{u}}^{\overline{I}} \\ \overline{\vartheta}^{\overline{I}} \end{bmatrix}, \tag{78}$$

for a macroscopic node $\overline{I}$. Using a matrix representation, the linearization can be formally written as

$$\mathrm{D}\overline{\mathbf{R}}^{\overline{E}} := \overline{\mathbf{S}}^{\overline{E}} : \Delta\overline{\mathbf{x}}^{\overline{E}} = \partial_{\overline{\mathbf{x}}^{\overline{E}}}\overline{\mathbf{R}}^{\overline{E}} : \Delta\overline{\mathbf{x}}^{\overline{E}}. \tag{79}$$

In order to obtain a consistent implementation for the macroscopic BVDH FE, Eqs. (55) and (56) are derived with respect to the nodal unknowns, defined in Eq. (78), which reads

$$\overline{\mathbf{S}}_{\overline{I}\overline{J}}^{\overline{E}} = \int_{\overline{\mathcal{B}}_{t_{\overline{E}}}} \frac{1}{v}\overline{\mathbf{N}}_b^{\overline{I}} \left[\partial_{\mathbf{x}_b}\mathbf{R}_b - \partial_{\mathbf{x}_a}\mathbf{R}_b : \partial_{\mathbf{R}_a}\mathbf{x}_a \, \partial_{\mathbf{x}_b}\mathbf{R}_a \right] \overline{\mathbf{N}}_b^{\overline{J}^T} \mathrm{d}\overline{v} + \overline{\mathbf{B}}_{\overline{I}\overline{J}}^{\overline{E}}, \tag{80}$$

after evaluating the implicit function theorem. Finally, the thermomechanical stiffness matrix with respect to the nodes $\overline{I}$ and $\overline{J}$ of a BVDH FE is obtained

$$\overline{\mathbf{S}}_{\overline{I}\overline{J}}^{\overline{E}} = \int_{\overline{\mathcal{B}}_{t_{\overline{E}}}} \frac{1}{v}\overline{\mathbf{N}}_b^{\overline{I}} \left[\mathbf{K}_{bb} - \mathbf{K}_{ba}\mathbf{K}_{aa}^{-1}\mathbf{K}_{ab} \right] \overline{\mathbf{N}}_b^{\overline{J}^T} \mathrm{d}\overline{v} + \overline{\mathbf{B}}_{\overline{I}\overline{J}}^{\overline{E}}, \tag{81}$$

where

$$\overline{\mathbf{B}}_{\overline{I}\overline{J}}^{\overline{E}}$$

$$:= \begin{bmatrix} -\int_{\partial\overline{\mathcal{B}}_{t_{\overline{E}\overline{t}}}} \overline{N}^{\overline{I}}\partial_{\overline{\boldsymbol{u}}^{\overline{J}}}(\overline{\boldsymbol{t}}\mathrm{d}\overline{a}) & -\int_{\partial\overline{\mathcal{B}}_{t_{\overline{E}\overline{t}}}} \overline{N}^{\overline{I}}\partial_{\overline{\vartheta}^{\overline{J}}}(\overline{\boldsymbol{t}}\mathrm{d}\overline{a}) \\ \int_{\partial\overline{\mathcal{B}}_{t_{\overline{E}\overline{q}}}} \overline{N}^{\overline{I}}\partial_{\overline{\boldsymbol{u}}^{\overline{J}}}(\overline{q}_n\mathrm{d}\overline{a}) & \int_{\partial\overline{\mathcal{B}}_{t_{\overline{E}\overline{q}}}} \overline{N}^{\overline{I}}\partial_{\overline{\vartheta}^{\overline{J}}}(\overline{q}_n\mathrm{d}\overline{a}) \end{bmatrix}, \tag{82}$$

contains the linearized boundary terms. The macroscopic overall FE solution can now be achieved by the assemblage of all macroscopic residuals and stiffnesses and the solution of

$$\left[\bigcup_{\overline{E}=1}^{\overline{N}} \overline{\mathbf{S}}^{\overline{E}} \right] : \left[\bigcup_{\overline{E}=1}^{\overline{N}} \Delta\overline{\mathbf{x}}^{\overline{E}} \right] + \left[\bigcup_{\overline{E}=1}^{\overline{N}} \overline{\mathbf{R}}^{\overline{E}} \right] = \mathbf{0}. \tag{83}$$

After having set the theoretical basis for an FE implementation, what remains is the description of an algorithmic treatment as Newton-type solution procedure.

2.2 Algorithmic treatment

The previous sections introduced the shape function $\overline{N}(\overline{\boldsymbol{\xi}}_b)$, that relates the appropriate RVE boundary node I to the macroscale element node $\overline{I}$. Recalling Eq. (8), this is based on the assumption of the natural scale relation between micro- and macroscale, due to their specific length scale ratio δ. Therefore, for every RVE boundary node, the natural coordinate $\overline{\boldsymbol{\xi}}_b$ needs to be determined in order that Eqs. (18) and (19) hold. In terms of an FEM solution procedure, this can be carried out in a preprocessing part and stored to be at hand for the solution of the micro and macro FE equations. Since the mapping in Eqs. (18) and (19) is not invertible, a local Newton procedure is carried out according to Algorithm 1. The implementation of the proposed computational homogenization scheme is of large importance, in order to obtain an FE solution of a heterogenous macrostructure. An algorithm for a three-dimensional thermomechanical BVDH element at finite strains is given in Algorithm 2.

3 Verification examples of BVDH

After having introduced BVDH, a comparison to common homogenization methods for different model examples concerning reliability and numerical efficiency is carried out. Since an analytical solution of the homogenization of small strain linear thermoelasticity for computing effective material properties is at hand, see [39], the first model problem is the comparison of BVDH to the numerical solution of such a type of problem as well as to the reference fine scale mesh solution. This comparison is made in order to verify BVDH solutions and to identify the reliability of them. Further verification examples are introduced by comparing BVDH to LDBCs, periodic displacement boundary conditions (PDBCs) and uniform traction boundary conditions (UTBCs) for three-dimensional mechanical finite deformation type of problems as described in [13]. This section closes with a comparative study on the influence of the mesh density and the length scale ratio δ onto the predictive capabilities of LDBC, PDBC and BVDH solutions at finite inelasticity.

3.1 One-dimensional thermoelasticity at small strains

This section investigates the predictive capabilities of BVDH in case of small strain and one-dimensional linear thermoelasticity. The model problem under investigation is schematically depicted in Fig. 3, where Fig. 3a shows the homogeneous and Fig. 3b the underlying heterogeneous

---

Algorithm 1 Determination of the macroscopic natural RVE coordinates $\bar{\boldsymbol{\xi}}_b$

---

require: known initial position of RVE boundary within macrostructure: $\overline{X}_R$
require: iteration counter: $k = 0$
ensure: initial estimate: $\bar{\boldsymbol{\xi}}_b^k$
compute initial position estimate $\overline{X}_{\mathrm{RVE}}(\bar{\boldsymbol{\xi}}_b^k) = \overline{N}(\bar{\boldsymbol{\xi}}_b^k)\overline{X}^E$
compute initial residual $\boldsymbol{R} = \overline{X}_R - \overline{X}_{\mathrm{RVE}}(\bar{\boldsymbol{\xi}}_b^k)$
while $\|\boldsymbol{R}\| >$ tolerance **do**
    compute position $\overline{X}_{\mathrm{RVE}}(\bar{\boldsymbol{\xi}}_b^k) = \overline{N}(\bar{\boldsymbol{\xi}}_b^k)\overline{X}^E$
    compute residual $\boldsymbol{R} = \overline{X}_R - \overline{X}_{\mathrm{RVE}}(\bar{\boldsymbol{\xi}}_b^k)$
    linearize $\mathrm{Lin}\boldsymbol{R} = \boldsymbol{R}|_{\bar{\boldsymbol{\xi}}_b^k} + \partial_{\bar{\boldsymbol{\xi}}_b}\boldsymbol{R}|_{\bar{\boldsymbol{\xi}}_b^k} : \Delta\bar{\boldsymbol{\xi}}_b$
    update $\Delta\bar{\boldsymbol{\xi}}_b = \bar{\boldsymbol{\xi}}_b^{k+1} - \bar{\boldsymbol{\xi}}_b^k$
    update $k = k + 1$
end while
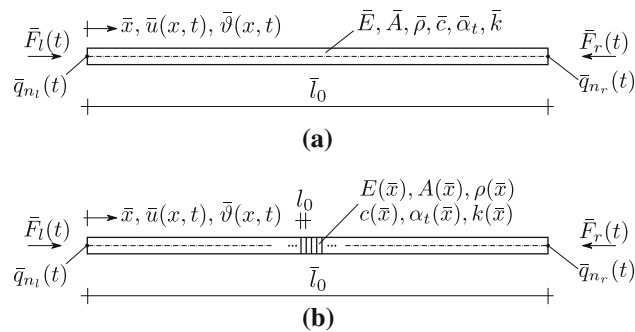
Fig. 3 Geometry and boundary conditions of a fully coupled thermomechanical linear one-dimensional rod. **a** Homogeneous model problem of one-dimensional rod. **b** Heterogeneous model problem of one-dimensional rod

model structure. Main focus of the considered model problem is the comparison against other solution methods. First alternative is the fine scale meshing and consideration of every single rod section, that has certain thermomechanical properties. The second alternative is a numerical investigation of an analytical homogenization solution of linear thermoelasticity, which is given in [39]. The homogenization of linear thermoelasticity in [39] is carried out such that, under the assumption of weakly converging displacements u of the fine scale to displacements $\bar{u}$ of the coarse scale for a length scale ratio δ tending to zero, effective parameters for the coarse scale can be computed. Considering the underlying heterogeneous model problem, compare Fig. 3b, the alternating thermomechanical properties, summarized in Table 1, are arbitrarily chosen. E denotes the Young's modulus, ρ represents the density, c is the mass specific heat capacity, $m = \sqrt{Ec\rho/\theta_0}$ is the thermoelastic coupling parameter and k represents the thermal conductivity. The parameters of lines 1 and 2 in Table 1 are alternating after 1 mm and are valid for a reference temperature of $\theta_0 = 293$ K. The total length $\bar{l}_0$ is taken to be 4 m and the cross-section is $\overline{A} = 0.1$ m^2. Thus, for the fine scale meshing solution 4000 ther-

momechanical linear displacement elements are considered. The semi-analytical solution procedure, which is a numerical computation based on the analytical solution given in [39], considers 160 of such elements, whose homogenized parameters are given in Table 2. The parameter w in Table 2, given in N/m^2 K, denotes the multiplication of the density ρ and the specific heat capacity c. These parameters are obtained as described in [39] and denote the effective parameters under consideration of a length scale ratio tending to zero. 160 thermomechanical linear displacement BVDH elements are also used to discretize the rod for a BVDH solution.

3.1.1 Excitation of the temperature field

The first model problem considered is an excitation of the temperature field at $\bar{x} = 0$ with a constant rate of $\dot{\bar{\vartheta}} = 5.0\mathrm{E}{-}06$ K/s for $1.0\mathrm{E}{+}06$ s, while the displacement field at $\bar{x} = 0$ is fixed. At $\bar{x} = \bar{l}_0$, the rod is isolated and the displacement is not fixed. The computed results for displacements $\bar{u}$ and reaction forces $\overline{F}$ are depicted in Fig. 4, where the continuous line represents the results of the reference fine scale solution and the dotted lines the homogenization results, which do overlap. As can be seen in Fig. 4a, the rod elongates in positive x direction for all the solution methods. In the context of heating, it is the expected result. The homogenization approaches are almost identical with the reference solution. This demonstrates the prediction capabilities of the semi-analytical and the BVDH approach in case of linear thermoelasticity. Figure 4b depicts the thermal power computed for the three alternative solution methods, measured at the fixed face of the rod. The results are again almost identical. Comparing the three alternatives, BVDH results show a reliable prediction of numerical solutions in time. The differences to the reference solution are almost negligible.

Algorithm 2 Thermomechanical BVDH element, $\overline{\mathcal{B}}_{t_{\overline{E}}}$

---

require: RVE geometry and material description
  positioning of $\mathcal{B}_{t_{\text{RVE}}}$ within $\overline{\mathcal{B}}_{t_{\overline{E}}}$ according to Eq. (7)
  compute local coordinates $\overline{\boldsymbol{\xi}}$ of RVE nodes according to Algorithm 1
  for $\overline{l} = 1$ to N_{SST} **do**   ▷ loop over N_{SST} RVEs
    for $E = 1$ to N **do**
      for $I = 1$ to $I^E \; \forall \, I \in \partial\mathcal{B}_{t_{\text{RVE}}}$ **do**
        get shape functions $\overline{\boldsymbol{N}}(\overline{\boldsymbol{\xi}})^I$
      end for
    end for
    for $E = 1$ to N **do**
      for $I = 1$ to $I^E \; \forall \, I \in \partial\mathcal{B}_{t_{\text{RVE}}}$ **do**
        interpolate displacements $\boldsymbol{u}(\boldsymbol{x},\, t)$ according to Eq. (18)
        interpolate temperature changes $\vartheta(\boldsymbol{x},\, t)$ according to Eq. (19)
      end for
    end for
    while $\| \boldsymbol{R}^T \| = \| [\boldsymbol{R}_{\text{mec}},\, \boldsymbol{R}_{\text{the}}]^T \| > \text{tol}$ **do**   ▷ iterate for RVE equilibrium
      for $E = 1$ to N **do**
        for $l = 1$ to L **do**   ▷ loop over L microscopic integration points
          get RVE material response, e.g. $\boldsymbol{\sigma}$, ρw_{ext}
        end for
      end for
      for $E = 1$ to N **do**
        for $l = 1$ to L **do**   ▷ loop over L microscopic integration points
          compute $\boldsymbol{R}^E$ contributions, see Eq. (45) and Eq. (46)
          compute $\boldsymbol{K}^E$ contributions, see Eq. (69)
        end for
      end for
      for $E = 1$ to N **do**
        assemble RVE residual $\boldsymbol{R}$, see Eq. (58)
        assemble RVE stiffness $\boldsymbol{K}$, see Eq. (73)
      end for
      solve $\boldsymbol{K}: \Delta[\boldsymbol{u},\, \vartheta]^T + \boldsymbol{R} = \boldsymbol{0}$, see Eq. (74)
      update $[\boldsymbol{u},\, \vartheta]^T$ by $\Delta[\boldsymbol{u},\, \vartheta]^T$
    end while
    compute $\overline{\boldsymbol{R}}_{\overline{l}}^{E}$ and $\overline{\boldsymbol{S}}_{\overline{l}}^{E}$ ▷ perform homogenization
  end for   ▷ end loop over N_{SST} RVEs
  compute $\overline{\boldsymbol{R}}^{E}$ from $\overline{\boldsymbol{R}}_{\overline{l}}^{E}$ and $\overline{\boldsymbol{S}}^{E}$ from $\overline{\boldsymbol{S}}_{\overline{l}}^{E}$, see Eq. (77) and Eq. (81)

Table 1 Model parameters for the fine scale solution and BVDH

	E (N/m^2)	ρ (kg/m^3)	c (J/kg K)	m (N/m^2 K)	k (W/mK)
1	7.00E10	2.50E6	8.70E2	4.56E5	2.36E2
2	7.08E5	2.61E3	9.00E1	4.66E2	2.50E0

Table 2 Model parameters for the semi-analytical solution

E (N/m^2)	ρ (kg/m^3)	w (N/m^2 K)	m (N/m^2 K)	k (W/mK)
1.41599E6	1.25130E6	1.08762E9	4.70948E2	4.94759E0

3.1.2 Excitation of the displacement field

The second model problem consists of an excitation of the displacement field of the rod depicted in Fig. 3. The underlying heterogeneous structure is again composed of the alternating thermomechanical properties, given in Table 1. The boundary conditions here are now set such that the displacement field $\overline{u}$ is fixed at $\overline{l} = \overline{l}_0 = 4$ m and prescribed with a constant compression rate of 10E$-$07 mm/s at $\overline{l} = 0$ for 10E+06 s. The temperature field $\overline{\vartheta}$ is isolated at $\overline{l} = \overline{l}_0 = 4$ m and fixed at $\overline{l} = 0$. The results obtained are depicted in Figs. 5 and 6. The first measured quantities are the displacements at $\overline{l} = \overline{l}_0/2 = 2$ m. Since the prescribed displacement at $\overline{l} = 4$ m is 0.1 m after 10E+06 s and in case of a pure mechanical problem, the geometrical and physical linearity of the problem would require $\overline{u} = 0.05$ m at $\overline{l} = 2$ m. Figure 5a depicts that all the different solution methods are nearly satisfying this requirement. The thermomechanical
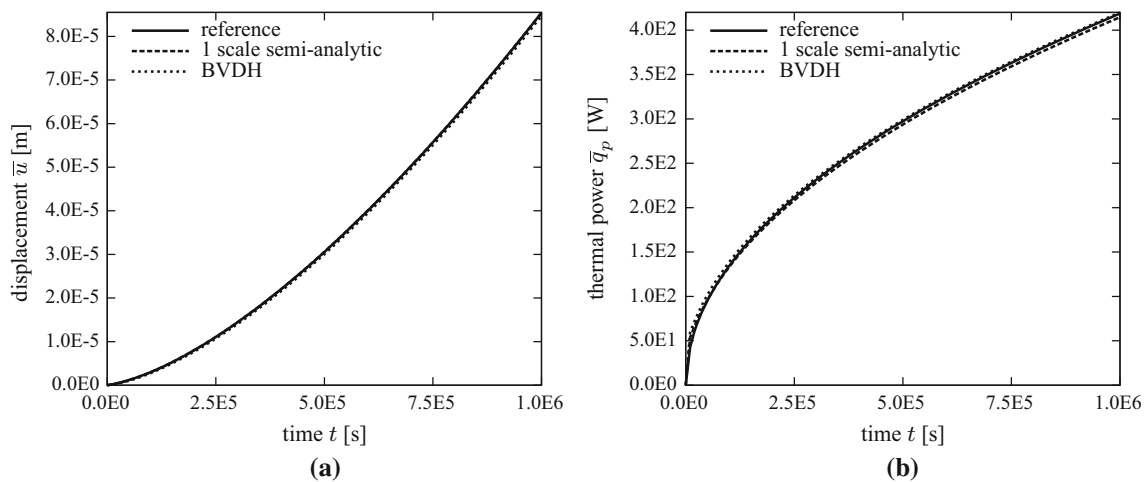
Fig. 4 Comparison of displacements $\bar{u}$ at $\bar{l} = 4$ m and thermal power $\bar{q}_p$ at $\bar{l} = 0$ for the reference, the one-scale semi-analytical and the BVDH solution
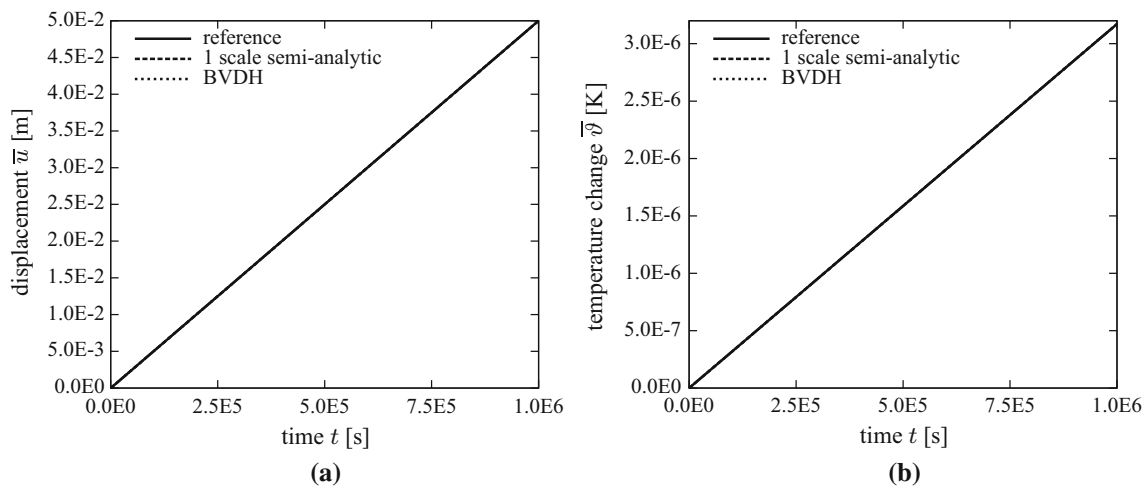

Fig. 5 Comparison of displacements $\bar{u}$ at $\bar{l} = \bar{l}_0/2$ and temperature changes $\bar{\vartheta}$ at $\bar{l} = \bar{l}_0/2$ for the reference, the one-scale semi-analytical and the BVDH solution

coupling and therewith the change of mechanical to thermal energy could cause slight differences compared to the pure mechanical solution. The heating of the rod at $\bar{l} = 2$ m is shown in Fig. 5b, which is expected since the rod is compressed. The identical solutions shown in Fig. 5 of the three different solution strategies are remarkable in context of the coupled PDE system of linear thermoelasticity. Thermal power and reaction forces for the considered problem are given in Fig. 6. Analyzing Fig. 6b and expecting a final reaction force at the fixed side of the rod with an absolute value of approximately $\overline{F} = (\overline{EA}/\bar{l}_0)\bar{u} \approx 3.54 \times 10^4$ N in case of a homogeneous mechanical rod, the dimension of the plotted reaction force time dependency is verified. The sign is negative since compression is considered. The computed thermal power $\bar{q}_p$ depicted in Fig. 6a shows almost no differences between the fine scale reference solution and both homogenization results. Concluding, the predictive capabilities

of BVDH and the semi-analytical approach are remarkable and reliable compared to a solution at the fine length scale.

3.2 Three-dimensional uniaxial tensile test

Next, a macroscopic uniaxial tensile test is carried out for a cubic specimen, having a heterogeneous microstructure. The considered problem is investigated with respect to reliability, taking into account the solutions obtained by BVDH, LDBC, PDBC and UTBC. The cubic macrostructure is discretized with 16 linear displacement elements in case of LDBC, PDBC and UTBC. At each of the integration points, the stresses and tangent moduli are computed as described in [13] in case of LDBC, PDBC and UTBC, respectively. The discretization in case of BVDH is carried out by 16 mechanical BVDH elements, similar to the thermomechani-
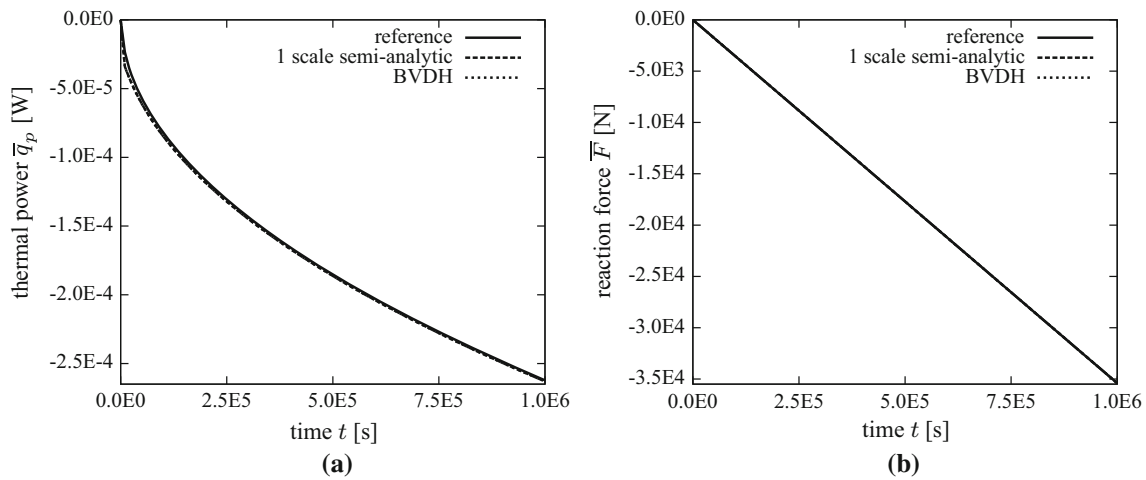
Fig. 6 Comparison of thermal power $\overline{q}_p$ at $\overline{l} = 0$ m and reaction force $\overline{F}$ at $\overline{l} = 4$ m for the reference, the one-scale semi-analytical and the BVDH solution
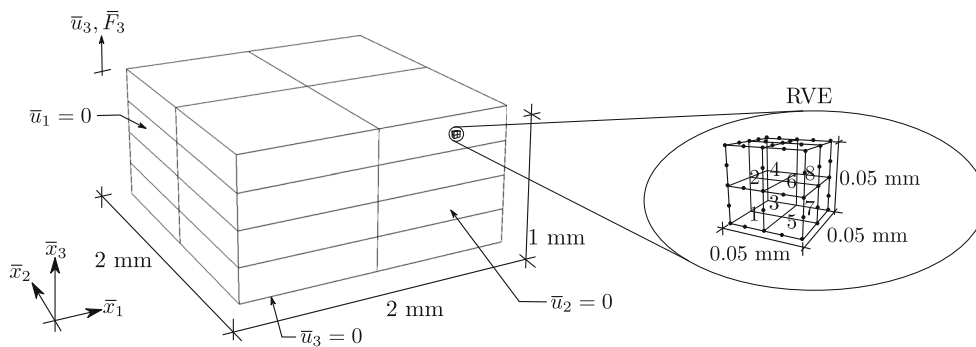
Fig. 7 Model example of heterogeneous cubic structure at homogeneous tensile test: geometry, boundary conditions and heterogeneous periodic microstructure (elements 1, 4, 6, 7 denoted by κ_1, μ_1 and elements 2, 3, 5, 8 denoted by κ_2, μ_2, see Table 3)

cal BVDH elements, described in Algorithm 2. The specific geometry of the macroscopic specimen is depicted in Fig. 7. The top surface is driven in global $\overline{x}_3$ direction with a constant velocity of $\dot{\overline{u}}_3 = 0.2$ mm/s for 10 s and the displacement boundary conditions are set, such that $\overline{u}_1(\overline{x}_1 = 0) = \overline{u}_2(\overline{x}_2 = 0) = \overline{u}_3(\overline{x}_3 = 0) = 0$. The related periodic RVE geometry is set to a cube with a side-length of 0.05 mm, which results in a length scale ratio of $\delta = 3.125 \times 10^{-5}$ and is discretized using 8 quadratic displacement elements having 20 nodes each, which results approximately in a distance of 0.01 mm between the RVE-nodes. The RVE size is chosen in order to obtain a quantitatively small number for the scale ratio. Time is discretized with 10 identical time steps $\Delta t = 1$ s. The RVE consists of two types of standard neo-Hooke-material, which is periodically alternating distributed within the microstructure as illustrated in Fig. 7. The different neo-Hooke parameters are arbitrarily chosen and given in Table 3. The resulting reaction forces are compared. The convergence behavior is investigated for each of the different solution methods.

Table 3 Model parameters of the RVE

	κ (MPa)	μ (MPa)
1	1500	655
2	1200	200

3.2.1 Comparison of reliability

As a comparable resulting quantity, the reaction force in global $\overline{x}_3$ direction of the driven top surface is summed up for all top nodes. The limits for the structural response obtained by BVDH are denoted by LDBC and UTBC, compare, e.g., [17]. Having a look at Fig. 8a, where the reaction forces of the four different approaches are plotted versus the prescribed displacements, one can recognize that LDBC reaction forces are larger and the values for the UTBC reaction forces are smaller than the ones obtained by BVDH. The first fact to discuss is the stiff result of LDBC compared to the less stiff result of UTBC. This fact denotes the two limits, which should not be violated by any physically meaningful homogenization result. The scale ratio at hand is $\delta = 3.125 \times 10^{-5}$
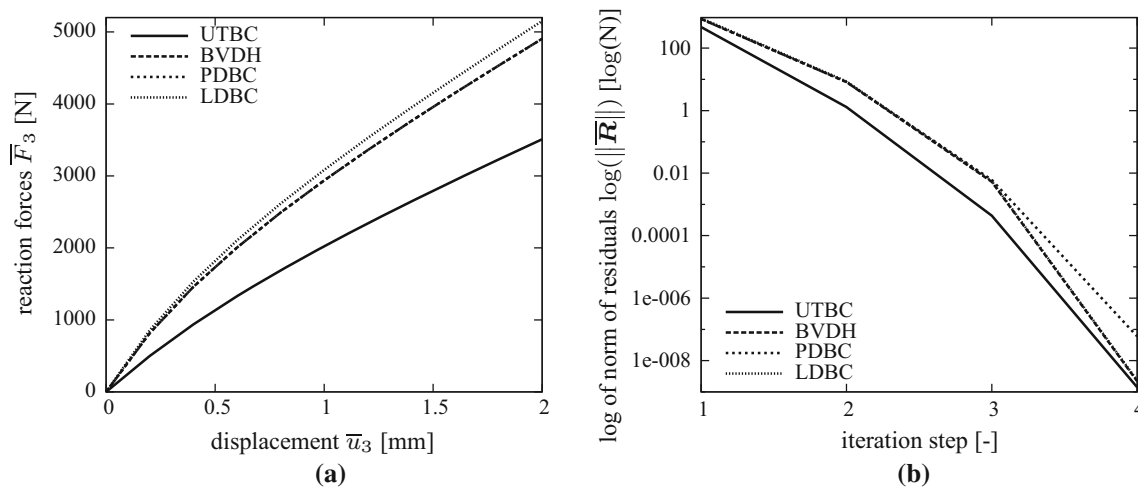
Fig. 8 Comparison of reaction force $\overline{F}_3$ of the prescribed displacement $\overline{u}_3$ at the top surface and comparison of the convergence behavior at $t = 10$ s for LDBC, UTBC, PDBC and BVDH for the homogeneous tensile test

Table 4 Norm of the residual of the convergence behavior for the tensile test with $\Delta t = 1.0$ s

Iteration steps (–)	BVDH $\|R\|$ (N)	LDBC $\|R\|$ (N)	PDBC $\|R\|$ (N)	UTBC $\|R\|$ (N)
1	8.60E+02	9.03E+02	8.60E+02	4.71E+02
2	8.16E+00	8.57E+00	8.16E+00	1.30E+00
3	5.27E−03	5.54E−03	6.08E−03	4.33E−04
4	2.20E−09	2.31E−09	5.99E−08	1.41E−09

in terms of a cubic RVE with a side length of 0.05 mm. Therewith, the second fact to discuss is the BVDH result. Recalling Sect. 3.1, where the reliability of BVDH is demonstrated for one-dimensional small strain problems, again the numerical solutions obtained by BVDH are within the physical range of computational homogenization, which can be seen in Fig. 8a. Analyzing Fig. 8b, one can state that all considered homogenization approaches converge superlinear with respect to the norm of the residual. This implies a correct algorithmic implementation. Table 4 depicts the specific values of the mechanical residual forces of the underlying tensile test at $t = 10$ s for the three different approaches. Figure 9 depicts the linearly deformed RVE shapes as well as their stress distribution at three different positions inside the macroscopic specimen during the BVDH computation. Having a close look at Fig. 9a, b, one can observe the non-homogeneous stress distribution, here with respect to σ_{33}, which is a result of the fully prescribed boundary data and the heterogeneous material structure inside the RVEs. The macroscopic homogeneous stresses ($\overline{\sigma}_{33}$) are depicted in Fig. 9c, d.

3.2.2 Comparison of efficiency

Evaluating the efficiency of the homogeneous tensile test, depicted in Fig. 7 for BVDH and three different boundary conditions of the homogenization approach introduced in [13], one can observe BVDH to be more efficient than the

two other cases. The quantities to compare, such as computation time of the results plotted in Fig. 8a, are given in Table 5. Having the same number of global iteration steps, BVDH is more than 3 times faster than LDBC, about 8 times faster than UTBC and approximately 11 times faster than PDBC, without loosing reliability. The reason for the reduced efficiency of the UTBC and PDBC homogenization schemes is the construction of the microscopic fluctuation field, which needs to be determined by additional boundary constraints. In both cases, an extra iteration needs to be introduced, compare [13], which causes an increase in computation time, in order to determine the microscopic fluctuation field based on the assumption of a uniform traction distribution as well as periodic displacements at the surface of the RVE. In case of LDBC, additional computations need to be carried out, in order to determine from the microscopic stresses and tangent moduli the macroscopic element residual and stiffness, compare [13]. In case of LDBC, PDBC and UTBC, the introduction of the microscopic fluctuation field leads to additional assumptions for the deformation of the surface of the RVE and causes an increase in computational costs.

3.3 Three-dimensional inhomogeneous compression test

Third, a macroscopic inhomogeneous compression test is carried out for a cubic specimen, considering first a periodic and second a non-periodic heterogeneous microstructure
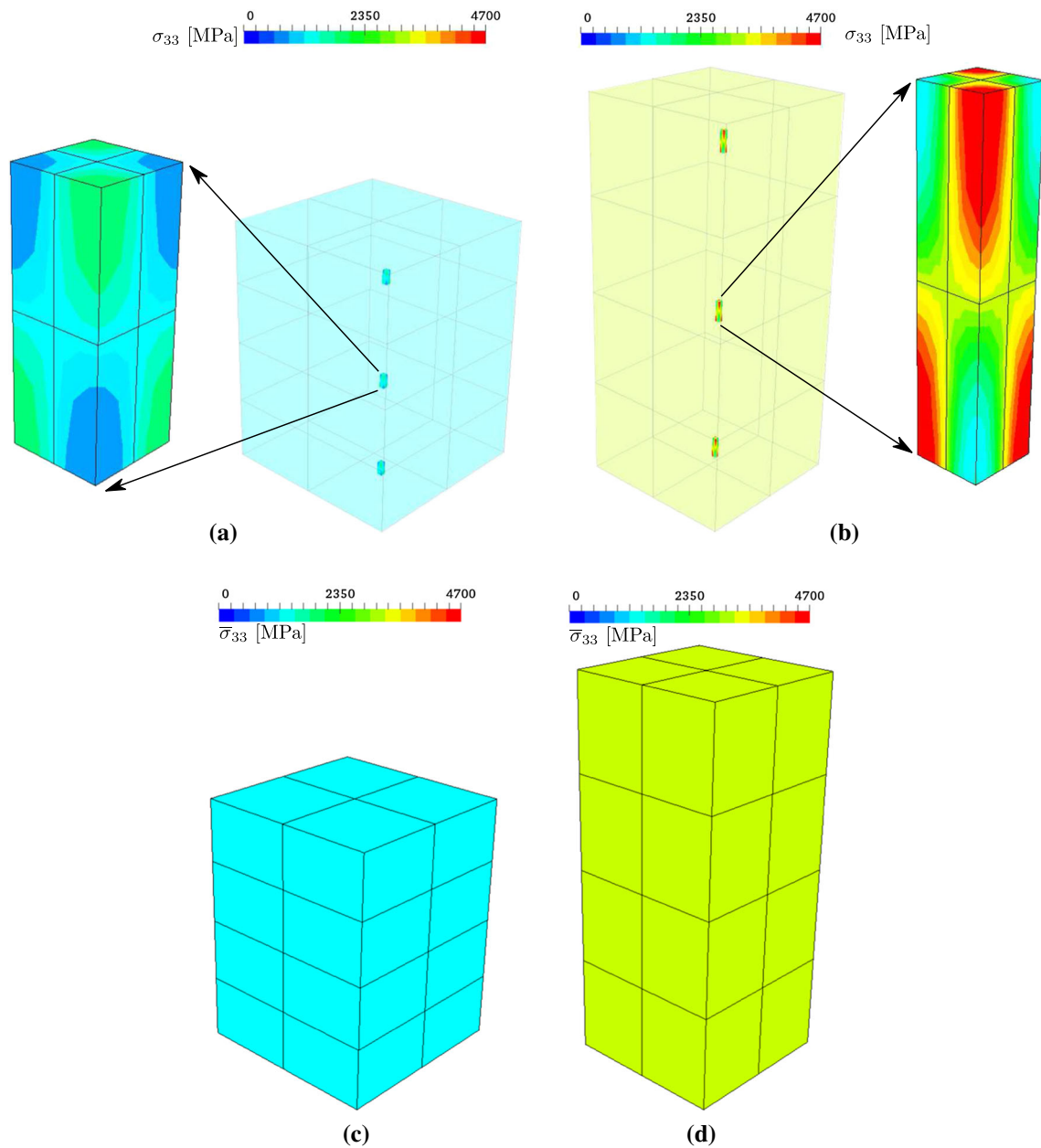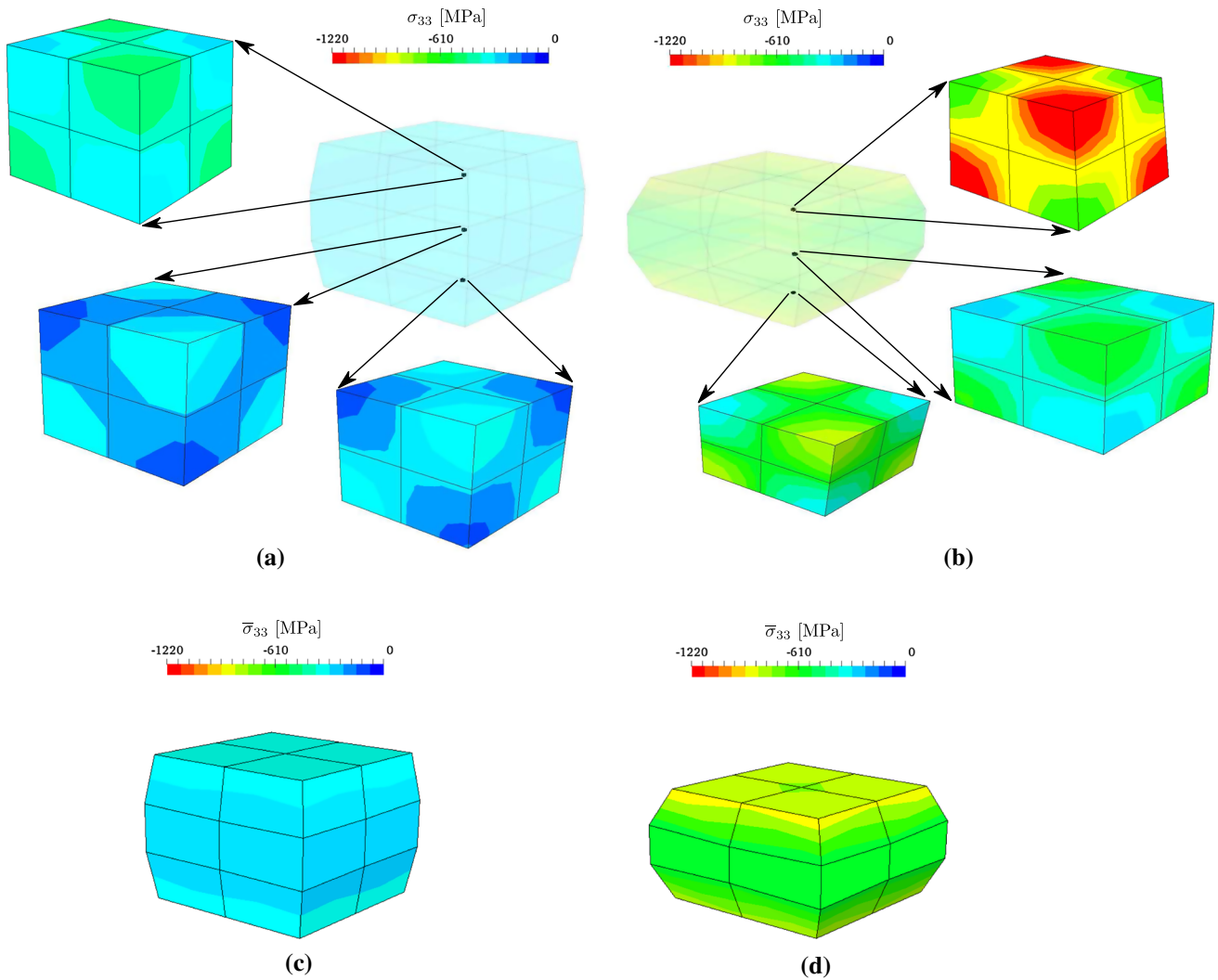
Fig. 9 Micro stresses at three specific RVEs and macroscopic stresses depicted at different times of the homogeneous tensile test for the BVDH solution. **a** σ_{33} at $t = 5.0$ s. **b** σ_{33} at $t = 10.0$ s. **c** $\bar{\sigma}_{33}$ at $t = 5.0$ s. **d** $\bar{\sigma}_{33}$ at $t = 10.0$ s s

Table 5 Comparison of efficiency with respect to different homogenization schemes for the homogeneous tensile test performed at four CPUs (Intel®Core™i7-4790 CPU: 3.60 GHz) in parallel with $\Delta t = 1$ s

Homogenization techniques	LDBC [13]	PDBC [13]	BVDH	UTBC [13]
Absolute computation time (s)	771.62	2727.46	248.53	1931.05
Relative computation time (%)	310	1097	100	777
Global iteration steps	40	40	40	40

similar to Sect. 3.2. The inhomogeneous compression test is investigated with respect to reliability and efficiency. Therefore, again a comparison of the solutions obtained by BVDH, LDBC, PDBC and UTBC is evaluated. The cubic macrostructure is discretized by 12 linear displacement elements in case of LDBC, PDBC and UTBC. At each of the integration points, the stresses and tangent moduli are computed as described in [13]. 12 mechanical BVDH elements
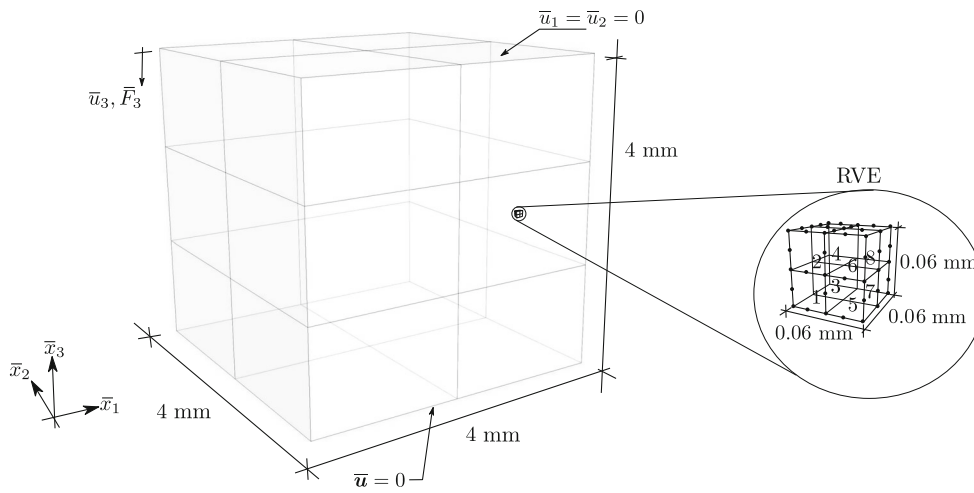
Fig. 10 Model example of a heterogeneous cubic structure at inhomogeneous compression test: geometry, boundary conditions and heterogeneous microstructure (periodic: elements 1, 4, 6, 7 denoted by κ_1, μ_1 and elements 2, 3, 5, 8 denoted by κ_2, μ_2; non-periodic: elements 1, 3, 4, 6, 7, 8 denoted by κ_1, μ_1 and elements 2, 5 denoted by κ_2, μ_2, see Table 3)
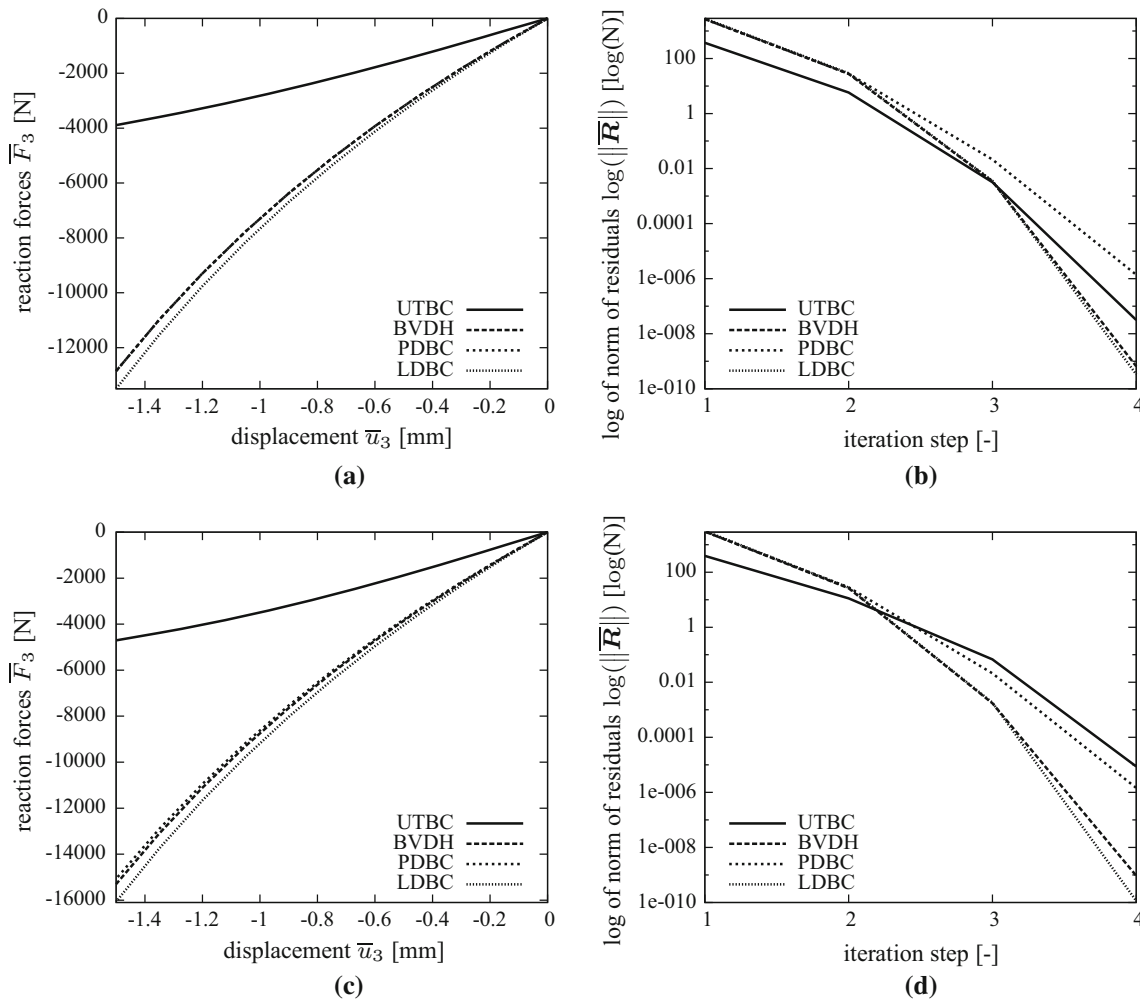
Fig. 11 Comparison of reaction force $\overline{F}_3$ of the prescribed displacement $\overline{u}_3$ at the top surface and comparison of the convergence behavior at $t = 10$ s for LDBC, UTBC, PDBC and BVDH for the inhomogeneous compression test. **a** Reaction force versus displacement *plot* for a periodic RVE. **b** Convergence behavior with a periodic RVE. **c** Reaction force versus displacement *plot* for a non-periodic RVE. **d** Convergence behavior with a non-periodic RVE

Table 6 Norm of the residual for the compression test with a periodic RVE ($\Delta t = 1.0$ s)

Iteration steps (–)	BVDH $\|\boldsymbol{R}\|$ (N)	LDBC $\|\boldsymbol{R}\|$ (N)	PDBC $\|\boldsymbol{R}\|$ (N)	UTBC $\|\boldsymbol{R}\|$ (N)
1	2.69E+03	2.82E+03	2.69E+03	3.72E+02
2	2.76E+01	2.90E+01	2.77E+01	5.76E+00
3	3.43E−03	3.60E−03	2.13E−02	3.20E−03
4	6.51E−10	3.34E−10	1.39E−06	3.15E−08

Fig. 12 Micro stresses of three specific RVEs and macroscopic stresses depicted at different times of the inhomogeneous compression test for the BVDH solution with a periodic microstructure. **a** σ_{33} at $t = 5.0$ s. **b** σ_{33} at $t = 10.0$ s. **c** $\bar{\sigma}_{33}$ at $t = 5.0$ s. **d** $\bar{\sigma}_{33}$ at $t = 10.0$ s

are used, in order to discretize the macrostructure, compare Algorithm 2. The specific geometry of the macroscopic specimen is depicted in Fig. 10. The top surface is driven in global $\bar{x}_3$ direction with a constant velocity of $\dot{\bar{u}}_3 = -0.15$ mm/s for 10 s, and the displacement boundary conditions are set, such that the top and bottom displacements are fixed. The related RVE geometry is a cube having a side length of 0.06 mm, which results now in a length scale ratio of $\delta = 3.375 \times 10^{-6}$ and is discretized using 8 quadratic displacement elements. Time is discretized by 10 identical time steps $\Delta t = 1.0$ s.

3.3.1 Comparison of reliability

As a comparable resulting quantity, the reaction force distribution in global $\bar{x}_3$ direction of the driven top surface is summed up for all top nodes. The reaction force-displacement dependency computed by LDBC denotes the stiffest structural behavior in terms of homogenization, while the softest structural response is obtained by UTBC. Having a look at Fig. 11a, where the reaction forces of the four different approaches are plotted versus the prescribed displacement for the periodic microstructure, one can recognize
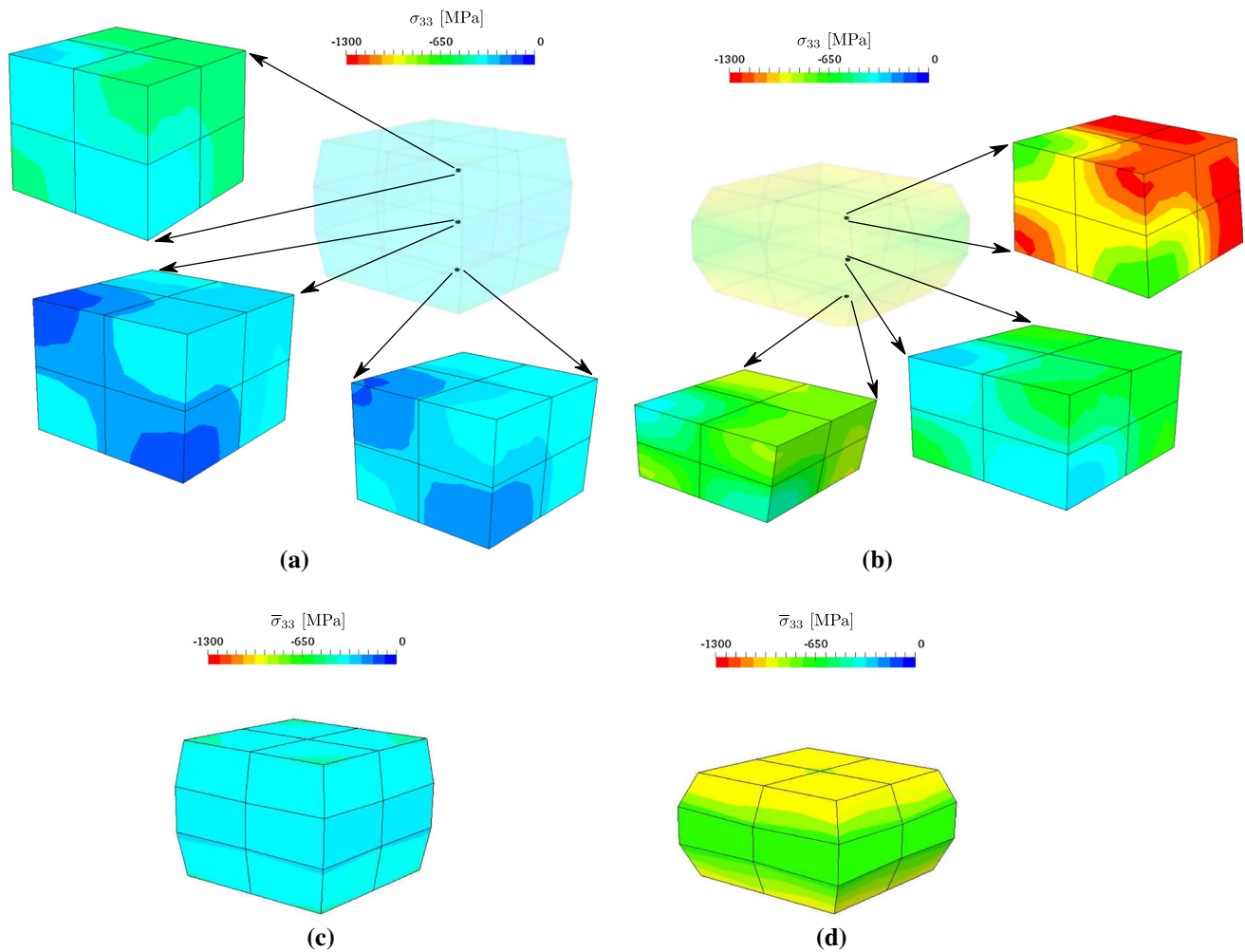
Fig. 13 Micro stresses of three specific RVEs and macroscopic stresses depicted at different times of the inhomogeneous compression test for the BVDH solution with a non-periodic microstructure. **a** σ_{33} at $t = 5.0$ s. **b** σ_{33} at $t = 10.0$ s. **c** $\bar{\sigma}_{33}$ at $t = 5.0$ s. **d** $\bar{\sigma}_{33}$ at $t = 10.0$ s

Table 7 Norm of the residual of the convergence behavior for the compression test with a non-periodic RVE ($\Delta t = 1.0$ s)

Iteration steps (–)	BVDH $\|R\|$ (N)	LDBC $\|R\|$ (N)	PDBC $\|R\|$ (N)	UTBC $\|R\|$ (N)
1	3.00E+03	3.15E+03	2.99E+03	3.93E+02
2	2.62E+01	2.76E+01	2.82E+01	1.12E+01
3	1.73E−03	1.81E−03	2.12E−02	6.80E−02
4	9.35E−10	1.15E−10	1.45E−06	8.77E−06

Table 8 Comparison of efficiency with respect to different homogenization schemes for the inhomogeneous compression test with a periodic microstructure performed at six CPUs (Intel®Core™i7-4790 CPU: 3.60 GHz) in parallel with $\Delta t = 1.0$ s

Homogenization techniques	LDBC [13]	PDBC [13]	BVDH	UTBC [13]
Absolute computation time (s)	438.72	1663.13	115.89	1406.30
Relative computation time (%)	378	1435	100	1213
Global iteration steps	40	40	40	40

that UTBC and LDBC are denoting the lower and upper bound for BVDH and PDBC, respectively. PDBC and BVDH are giving identical results with respect to the periodicity of the RVE. Comparing Fig. 11a, c, BVDH and PDBC are not anymore overlapping. With increasing deformation, PDBC results in a less stiffer structural response, while BVDH tends to compute stiffer reaction forces for the identical macroscopic model problem. It should be noted, that the problem

Table 9 Comparison of efficiency with respect to different homogenization schemes for the inhomogeneous compression test with a non-periodic microstructure performed at six CPUs in parallel ($\Delta t = 1.0$ s)

Homogenization techniques	LDBC [13]	PDBC [13]	BVDH	UTBC [13]
Absolute computation time (s)	440.23	1840.47	116.90	1391.45
Relative computation time (%)	376	1574	100	1190
Global iteration steps	40	40	40	40

(a)

(b)
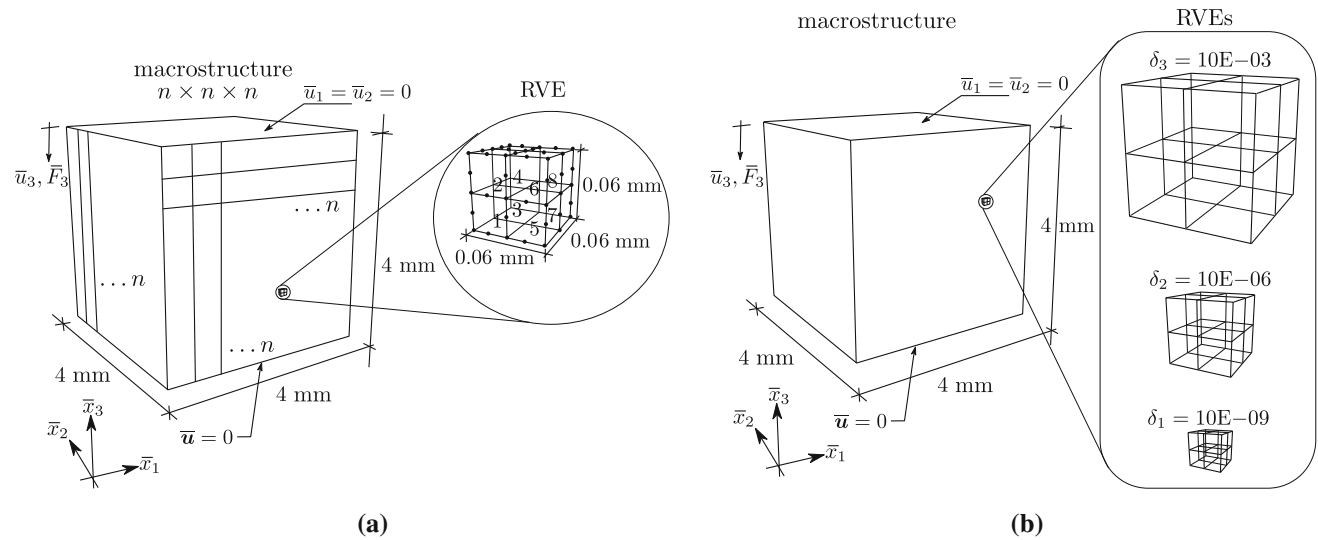
Fig. 14 Model example of a heterogeneous cubic structure at inhomogeneous compression test: geometry, boundary conditions and inelastic heterogeneous microstructure (non-periodic: elements 1, 3, 4, 6, 7, 8 denoted by material 1 and elements 2, 5 denoted by material 2, see Table 10). **a** Model setup of mesh density investigations. **b** Model setup of length scale ratio investigations

considered is of academic nature. Industry related and more complex problems might cause larger differences between all four homogenization techniques. Similar to the previous tensile test, all three solution techniques converge globally at least superlinear to a zero residual of the difference between external and internal force contributions, as depicted in Fig. 11b, d. The residual forces are explicitly given in Table 6. Figure 12 illustrates different stress states for different times of the micro- and the macroscale with a periodic RVE, while Fig. 13 depicts the appropriate micro- and macroscale situations with the non-periodic RVE. Table 7 contains the norm of the residual forces while iteration for the macroscale including a non-periodic RVE. As depicted, the RVEs are characterized by an inhomogeneous stress state and its approximate mean value yields the homogenized macroscopic stress state, compare Eq. (39).

3.3.2 Comparison of efficiency

Evaluating the efficiency of the inhomogeneous compression test containing a periodic and a non-periodic microstructure as depicted in Fig. 10, again for BVDH and three different boundary conditions of a common homogenization method, one can observe BVDH to be more efficient than the other

Table 10 Model parameters of the heterogeneous inelastic RVE

	κ (MPa)	μ (MPa)	σ_y (MPa)	$\dot{\gamma}_0^p$ (1/s)
Material 1	1500	655	200	5.0E−05
Material 2	1200	200	100	7.0E−05

cases. The efficiency measures to compare, such as computation time of the results plotted in Fig. 11a, c, are given in Tables 8 and 9, respectively.

3.4 Mesh density dependency

In order to study the influence of the mesh quality and mesh density on the structural results of the displacement driven homogenization methods, the example of the inhomogeneous compression test with a non-periodic microstructure is considered, see Fig. 14. The discretization is carried out with the density factor n, such that a mesh of a regular structure $n \times n \times n$ is realized, see Fig. 14a. The macroscopic boundary conditions as well as the geometry are given in Fig. 14 and are constant for all differently tested mesh density factors n. The top displacement $\overline{u}_3 = -1.5$ mm is applied in 10 s for constant time steps of 1 s. The constitutive model used with different parameters for materials 1 and 2 (see Table
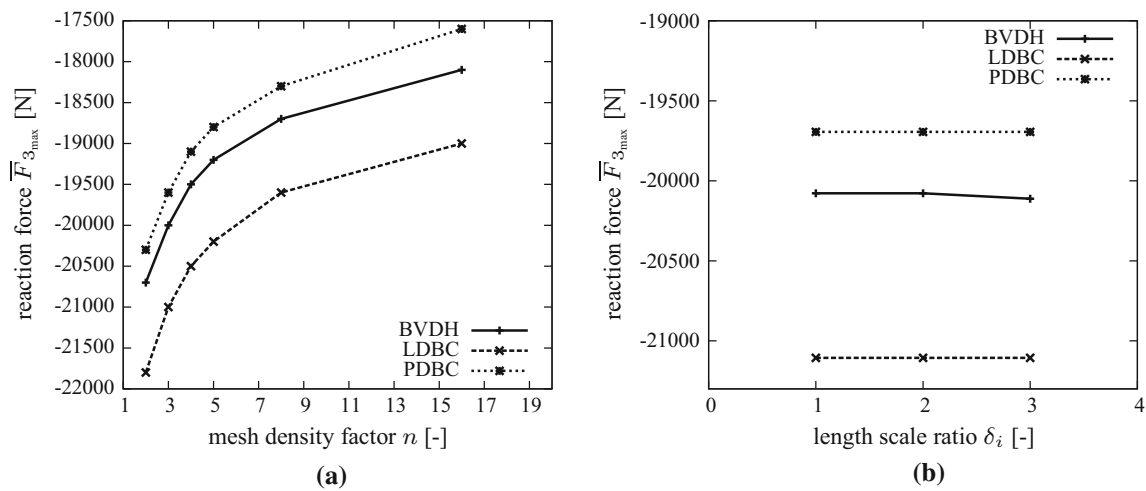
Fig. 15 Comparison of maximum of the reaction force $\overline{F}_3$ of the prescribed displacement $\overline{u}_3$ at the top surface with respect to different mesh densities and length scale ratios for the displacement dependent homogenization techniques PDBC, LDBC and BVDH, respectively. **a** Reaction force versus mesh density factor. **b** Reaction force versus length scale ratio
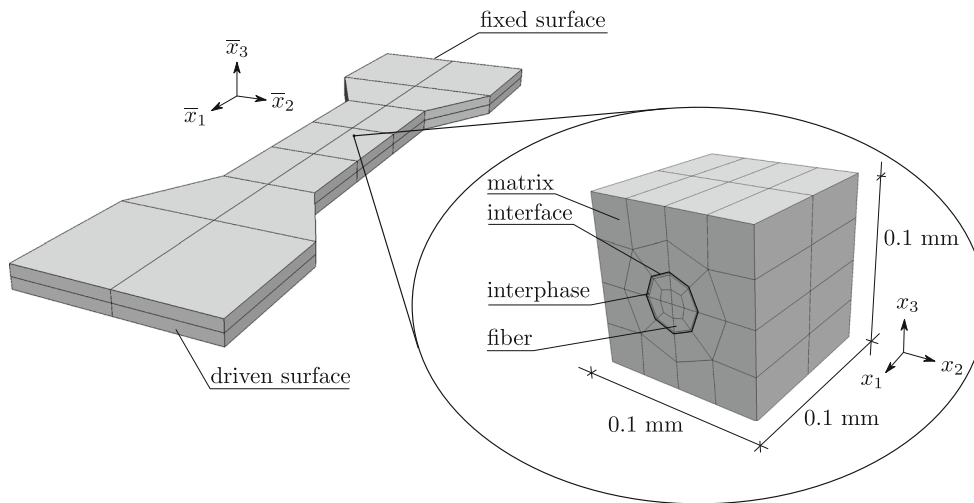

Fig. 16 Geometry and discretization of the macroscopic tensile test specimen according to [41] and the RVE geometry as well as discretization for the fiber direction dependent uniaxial tensile test

Table 11 Identified model parameters of the RVE

	κ (MPa)	μ (MPa)	$\dot{\gamma}_0$ (1/s)	s_{ss} (MPa)	h (MPa)	c_1 (MPa)
Polyamide	5620	1600	8.0E+16	170	300	2
	c_2 (MPa)	α_t (1/K)	k (W/mK)	$\hat{c}$ (N/K mm^2)	ΔG (J)	s_0 (MPa)
Polyamide	-0.05	2.E-6	0.23	1.3	2.4E-19	195
	κ (MPa)	μ (MPa)	α_t (1/K)	k (W/mK)	$\hat{c}$ (N/K mm^2)	
Glass-fiber	43,500	28,646	1.0E-6	0.5	1	
	κ_s (N/mm^3)	η_d (N/mm)	k_c (N/mm^3)	α_t (1/K)	k (W/mK)	
Interface	20	23.6	1.0E+5	2.E-6	1.3	

10) is an elasto-plastic model, suitable for finite deformations and is based on the developments made in [40]. In [40], semicrystalline polymers are constitutively described by separately modeling their amorphous and their crystalline phase. The model applied in the investigation at hand is based on the elasto-plastic model for the crystalline part, see [40]. All different homogenization methods and their maximum compressive force are asymptotically converging to a steady state value, as shown in Fig. 15a. This fact corresponds to the typical h-convergence behavior of finite displacement elements. Concluding, it can be noted, that with increasing mesh density, the different homogenization methods tend to different asymptotes.

3.5 Length scale ratio dependency

In order to study the influence of the length scale ratio $\delta = v/\overline{v}$ on the structural results of the displacement driven homogenization methods, the example of the inhomogeneous compression test with a non-periodic microstructure is considered. The macroscopic boundary conditions, the discretization as well as the geometry are given in Fig. 14b and are constant for all differently tested scale ratios δ_i. The top displacement $\overline{u}_3 = -1.5$ mm is applied in 10 s for equal time steps of 1 s. The non-periodic RVE is considered with two different inelastic materials similar to the elasto-plastic model developed in [40], see Sect. 3.4.

As shown in Fig. 15b, LDBC and PDBC are independent of the scaling of the RVE size, as long as the structure of the RVE does not change, compare Sect. 3.3. In case of the influence of δ on the BVDH solutions, a slight decrease of reaction forces with increasing δ can be recognized, see Fig. 15b. The macroscopic discretization yields the limit for the maximum length scale ratio with respect to BVDH, since the RVEs of a macroscopic BVDH-element (see Algorithms 1 and 2) have to completely fit into the macroscopic element. This restriction follows from the kinematical assumptions (see Sect. 2.1.1) and has to be accepted due to the fact, that otherwise the application of a homogenization method does not make sense. But the scale ratio dependent results for $\overline{F}_{3_{\max}}$ with respect to BVDH are acceptable with regard to Eq. (39). The independency of LDBC and PDBC solutions from δ similarly arises from the volume averaging, see Eq. (39) and the assumption of considering RVEs as macroscopic points without a direct scale relation. The differences between each homogenization method can be explained in the context of the different procedures of homogenizing the microstructural properties.

4 Application example of BVDH

The final predictive example is a numerical investigation of a macroscopic uniaxial tensile test specimen, see [41]. Fig-
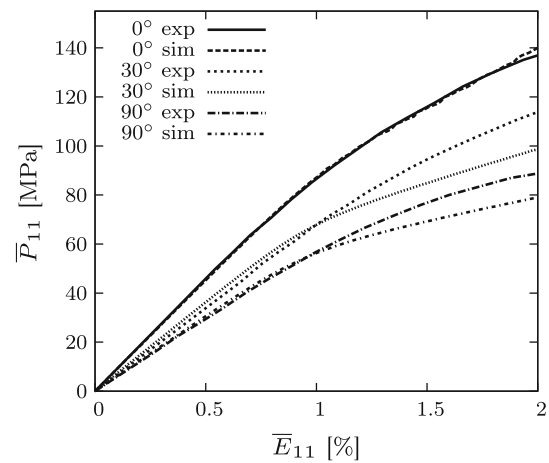

Fig. 17 Comparison of engineering stress strain relations of experimental investigations (taken from [41]) and numerical simulations using BVDH for different fiber orientations

ure 16 depicts the geometry and the discretization of the macroscopic specimen, which represents a short-glass-fiber reinforced thermoplastic (polyamide PA66GF35). Only a quarter or a half of the specimen is discretized due to single-symmetry or double-symmetry of the structure with respect to the fiber-orientations of 0°, 30° and 90°.

As stated in Sect. 2, one advantage of homogenization approaches is the reduced discretization workload. Hence, the macroscopic specimen is discretized using 7 or 14 thermomechanical BVDH elements, as described in Sect. 2.2 and by Algorithm 2. The test investigated is carried out at a constant tensile speed of 0.3 mm/min and the resulting displacements are applied to the driven surface. The opposite surface is fixed with respect to the displacements. The boundary conditions for the temperature field are set to free surfaces, since no thermal isolation is assumed. No convection to the surrounding environmental temperature is assumed at the macroscopic scale. The RVE is chosen to have a cubic geometry with a volume $v = 0.001$ mm³. The discretization of the RVE is carried out by 80 linear thermomechanical elements for the bulk materials, such as matrix, fiber and interphase and by 16 thermomechanical interface elements according to [42] for the designated failure layer between interphase and matrix. The constitutive description of the thermoplastic matrix material polyamide PA66GF35 and the interphase treatment are taken from [43]. The glass-fiber material is modeled according to [44] as a thermoelastic neo-Hooke material. The RVE geometry and material description represent a glass fiber reinforced polyamide thermoplastic with approximately 3.5 % fiber content. The model parameters are identified using the uniaxial tensile test for a fiber orientation of 0° and verified at fiber orientations of 30° and 90° with respect to the tensile direction. The full model parameter set is given in Table 11. Figure

Fig. 18 Macro stresses and micro stresses of the investigated structure for a fiber orientation of 0° at a macroscopic engineering strain of 2 % at the middle of the neck
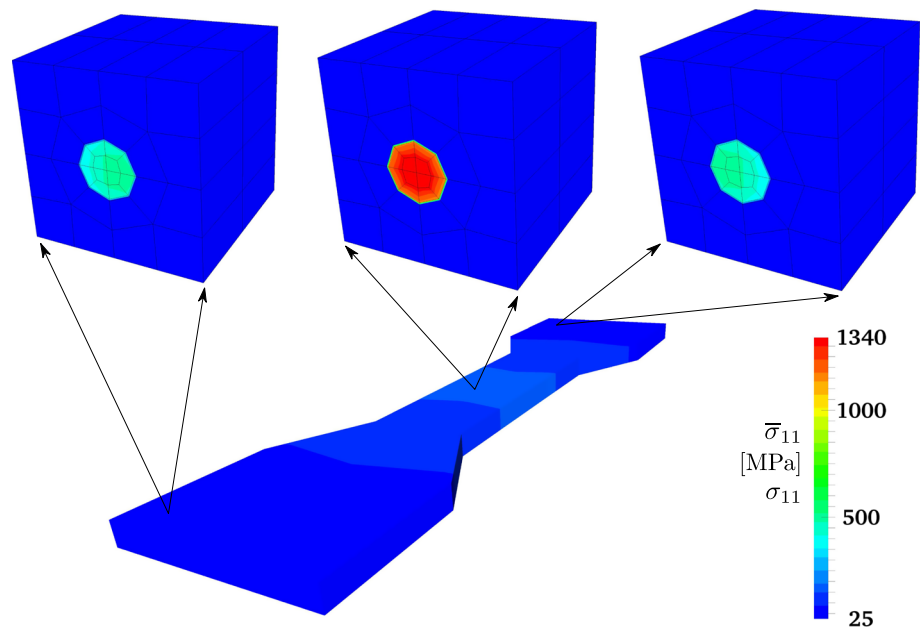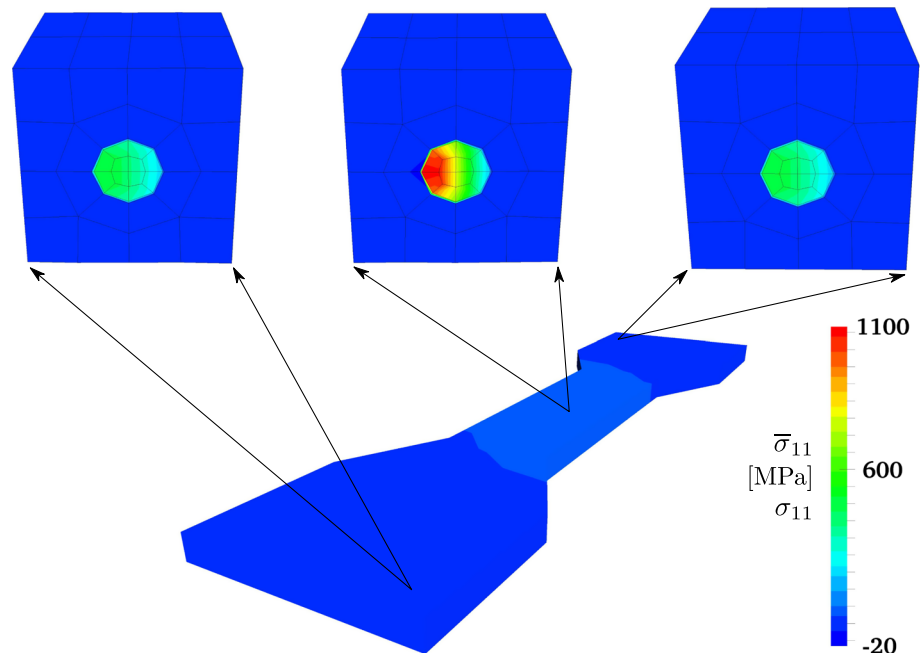

Fig. 19 Macro stresses and micro stresses of the investigated structure for a fiber orientation of 30° at a macroscopic engineering strain of 2 % at the middle of the neck


17 depicts the resulting engineering stresses versus engineering strains in tensile direction evaluated at the middle of the neck of the macroscopic specimen for the three fiber orientations. As can be seen in Fig. 17, the simulation results are in acceptable agreement with the experimental results. Since the parameter identification is carried out at small strains, where the materials are undergoing almost only elastic deformations, mainly the elastic constants of the different materials are identifiable. The remaining inelastic parameters of polyamide are assumed to be similar to polymethylmethacrylate and are based on the parametric study in [45].

The differences between simulations and experiments in the range of 1–2 % strain for fiber directions of 30° and 90°, see Fig. 17, are having different reasons. The first reason is the lack of information about the inelastic behavior of PA66GF35 as exclusive bulk material, which results in a parameter identification for the composite. Second, the preparation of the test specimens, as described in [41], does not ensure a perfect fiber orientation for every single short-fiber in every orientation case, compared to the numerical investigations. The experiments are carried out at least three times with respect to the uniaxial tensile tests for every fiber orientation and dis-

Fig. 20 Macro stresses and micro stresses of the investigated structure for a fiber orientation of 90° at a macroscopic engineering strain of 2 % at the middle of the neck
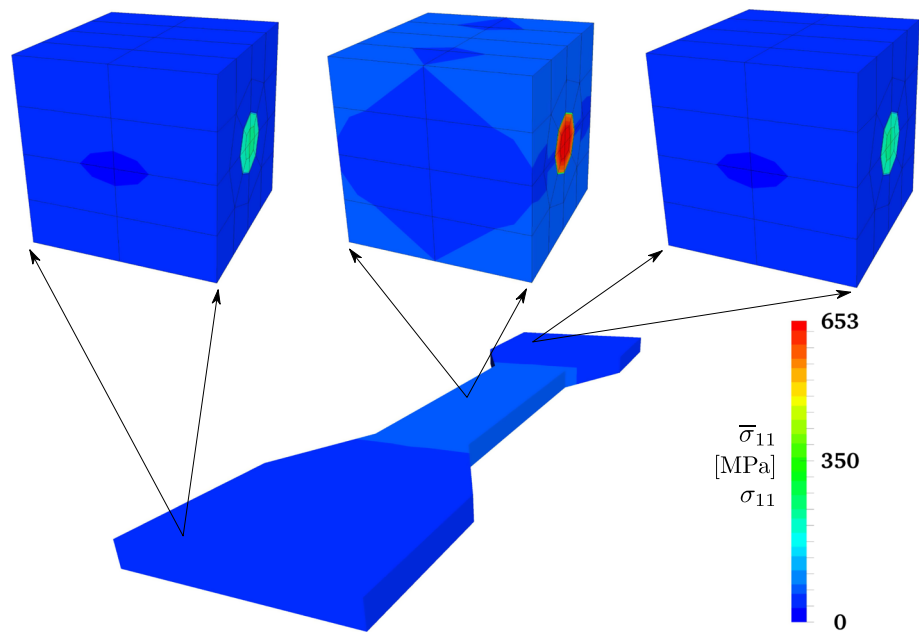
Fig. 21 Temperature distribution of the investigated structure for a fiber orientation of 0° at a macroscopic engineering strain of 2 % at the middle of the neck
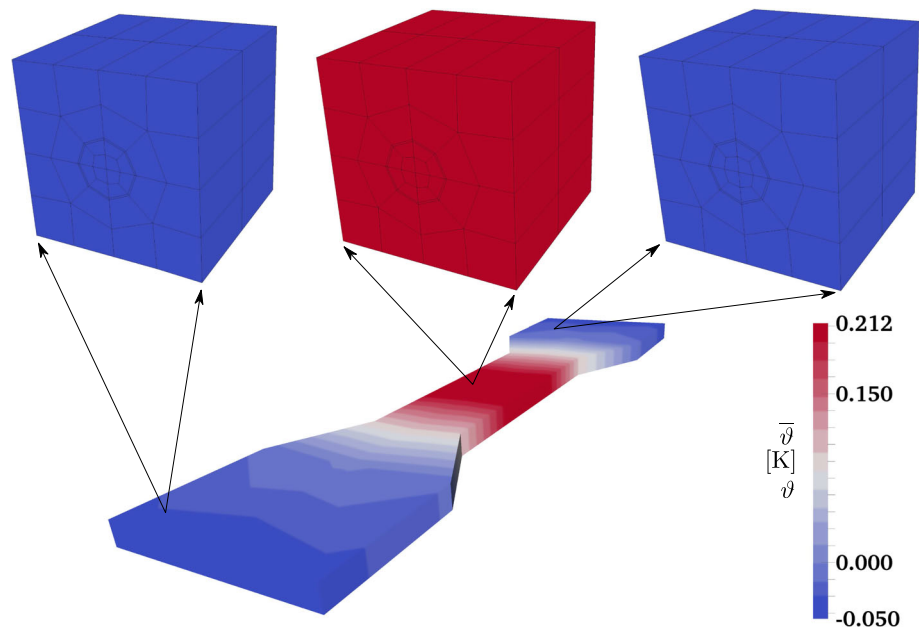
placement rate, as stated in [41]. The resulting uncertainty of data is not considered in the numerical simulations. The macroscopic stress distribution and the related microscopic stresses of specific RVEs are depicted in Figs. 18, 19 and 20. The plots are depicting an engineering strain of 2 % at the middle of the neck. As can be seen from these figures, the stresses decrease in the neck of the specimen as the fiber orientation changes from 0° to 90°, which is plausible due to the reduced stiffness in tensile direction. Additionally, it is recognizable, that the macroscopic stress distribution follows the fiber orientation. Mainly, the fiber reinforcements are car-

rying the tensile loads as can be seen from the RVE stress distributions due to their large stiffness. The related temperature distributions for the three different fiber orientations of the specimen as well as of three specific RVEs are depicted in Figs. 21, 22 and 23. The neck heats up, due to dissipative phenomena of the inelastic matrix material, while the parts of the specimen, which are still within the elastic stress range or start to develop inelastic deformation, are denoted by the entropic cooling under tension or slightly heat up, respectively. The specific RVE temperature changes are within the range of the surrounding macroscopic temperature changes.

Fig. 22 Temperature distribution of the investigated structure for a fiber orientation of 30° at a macroscopic engineering strain of 2 % at the middle of the neck
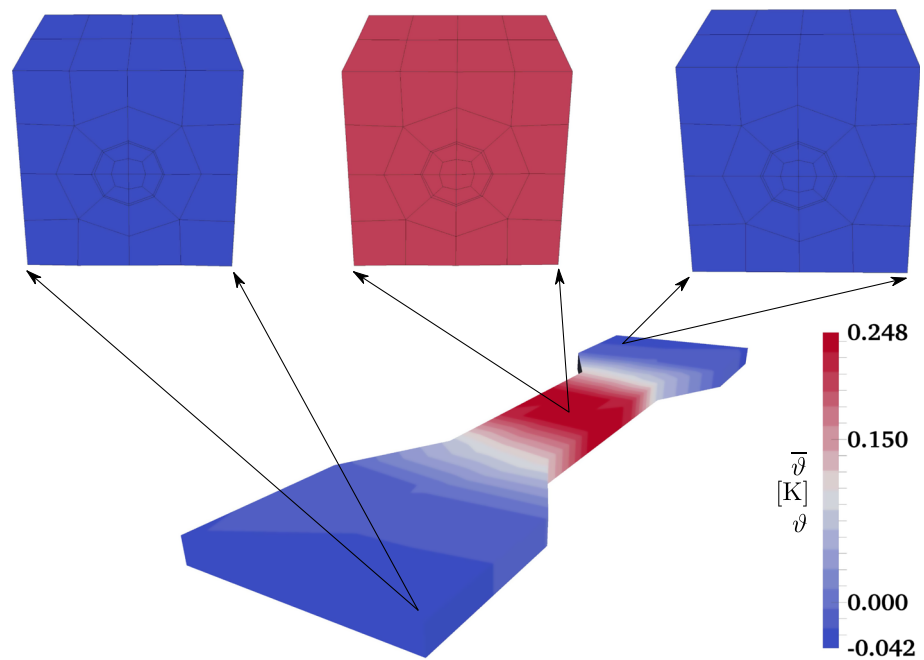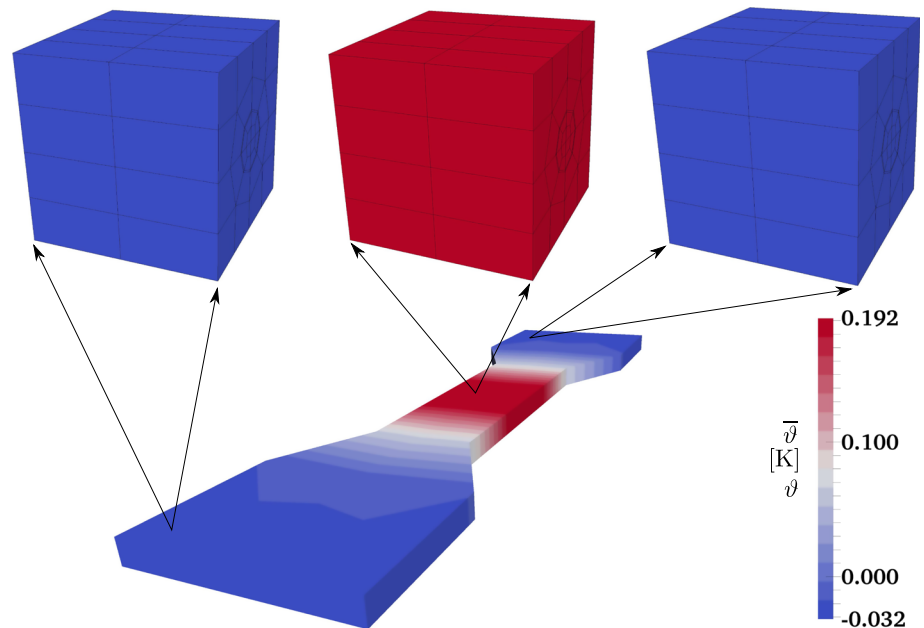

Fig. 23 Temperature distribution of the investigated structure for a fiber orientation of 90° at a macroscopic engineering strain of 2 % at the middle of the neck

5 Conclusion and outlook

A novel multiphysical homogenization method (BVDH), suitable for fully coupled thermomechanical problems, is developed and consistently treated for use within an FEM framework. The reliability of BVDH solutions is verified for semi-analytical and reference solutions, and its efficiency is also successfully proved against standard computational homogenization. The applicability of BVDH is demonstrated for structural investigations by comparing simulation results to experimental investigations. Dynamic loadings and resulting inertia effects can be considered using BVDH for structural applications. An investigation of the reliability and efficiency of BVDH regarding these effects will be carried out in future research. Focus will also be set on localization of deformation phenomena at dynamic loadings of inelastic heterogenous solids. Thus, the dynamic BVDH reliability needs to be verified for different time integration procedures, e.g., implicit or explicit methods. It would also be interesting to investigate the predictive capabilities of BVDH for field theories other than thermomechanics, e.g., electro-mechanics.

References

1. Geers MGD, Kouznetsova VG, Brekelmans WAM (2010) Multi-scale computational homogenization: trends and challenges. J Comput Appl Math 234:2175

2. Kanouté P, Boso DP, Chaboche JL, Schrefler BA (2009) Multiscale methods for composites: a review. Arch Comput Methods Eng 16:31

3. E W, Engquist B, Li X, Ren W, Vanden-Eijnden E (2007) Heterogeneous multiscale methods: a review. Commun Comput Phys 2:367

4. Babuška I, Andersson B, Smith P, Levin K (1999) Damage analysis of fiber composites—Part I. Statistical analysis on fiber scale. Comput Methods Appl Mech Eng 172:27

5. Temizer I, Wu T, Wriggers P (2013) On the optimality of the window method in computational homogenization. Int J Eng Sci 64:66

6. Terada K, Hirayama N, Yamamoto K, Muramatsu M, Matsubara S, Nishi S (2016) Numerical plate testing for linear two-scale analyses of composite plates with in-plane periodicity. Int J Numer Methods Eng 105:111

7. Temizer I, Wriggers P (2007) An adaptive method for homogenization in orthotropic nonlinear elasticity. Comput Methods Appl Mech Eng 196:3409

8. Ghosh S, Lee K, Moorthy S (1995) Multiple scale analysis of heterogeneous elastic structures using homogenization theory and Voronoi cell finite element method. Int J Solids Struct 32:27

9. Guedes JM, Kikuchi N (1990) Preprocessing and postprocessing for materials based on the homogenization method with adaptive finite element methods. Comput Methods Appl Mech Eng 83:143

10. Coenen EWC, Kouznetsova VG, Geers MGD (2012) Novel boundary conditions for strain localization analyses in microstructural volume elements. Int J Numer Methods Eng 90:1

11. Kouznetsova V, Brekelmans WAM, Baaijens FPT (2001) An approach to micro–macro modeling of heterogeneous materials. Comput Mech 27:37

12. Miehe C (2002) Strain-driven homogenization of inelastic microstructures and composites based on an incremental variational formulation. Int J Numer Methods Eng 55:1285

13. Miehe C (2003) Computational micro-to-macro transitions for discretized micro-structures of heterogeneous materials at finite strains based on the minimization of averaged incremental energy. Comput Methods Appl Mech Eng 192:559

14. Miehe C, Lambrecht M, Schotte J (2001) Computational homogenization of materials with microstructure based on incremental variational formulations. In: Miehe C (ed) IUTAM symposium on computational mechanics of solid materials at large strains. Kluwer Academic Publishers, Dordrecht

15. Miehe C, Schotte J, Lambrecht M (2002) Homogenization of inelastic solid materials at finite strains based on incremental minimization principles. Application to the texture analysis of polycrystals. J Mech Phys Solids 50:2123

16. Miehe C, Schröder J, Schotte J (1999) Computational homogenization analysis in finite plasticity simulation of texture development in polycrystalline materials. Comput Methods Appl Mech Eng 171:387

17. Terada K, Hori M, Kyoya T, Kikuchi N (2000) Simulation of the multi-scale convergence in computational homogenization approaches. Int J Solids Struct 37:2285

18. Geers M, Kouznetsova VG, Brekelmans WAM (2003) Multi-scale first-order and second-order computational homogenization of microstructures towards continua. Int J Multiscale Comput Eng 1:371

19. Kouznetsova V, Geers MGD, Brekelmans WAM (2002) Multi-scale constitutive modelling of heterogeneous materials with a gradient-enhanced computational homogenization scheme. Int J Numer Methods Eng 54:1235

20. Kouznetsova V, Geers M, Brekelmans W (2004) Multi-scale second-order computational homogenization of multi-phase materials: a nested finite element solution strategy. Comput Methods Appl Mech Eng 193:5525

21. Temizer I, Wriggers P (2008) On the computation of the macroscopic tangent for multiscale volumetric homogenization problems. Comput Methods Appl Mech Eng 198:495

22. Ibrahimbegović A, Markovič D (2003) Strong coupling methods in multi-phase and multi-scale modeling of inelastic behavior of heterogeneous structures. Comput Methods Appl Mech Eng 192:3089

23. Zhang HW, Wu JK, Lv J (2012) A new multiscale computational elasto-plastic analysis of heterogeneous materials. Comput Mech 49:149

24. Özdemir I, Brekelmans WAM, Geers MGD (2008) FE^2 computational homogenization for the thermo-mechanical analysis of heterogeneous solids. Comput Methods Appl Mech Eng 198:602

25. Mandadapu KK, Sengupta A, Papadopoulos P (2012) A homogenization method for thermomechanical continua using extensive physical quantities. Proc R Soc A 468:1696

26. Terada K, Kurumatani M, Ushida T, Kikuchi N (2010) A method of two-scale thermo-mechanical analysis for porous solids with micro-scale heat transfer. Comput Mech 46:269

27. Monteiro E, Yvonnet J, He QC (2008) Computational homogenization for nonlinear conduction in heterogeneous materials using model reduction. Comput Mater Sci 42:704

28. Temizer I, Wriggers P (2011) Homogenization in finite thermoelasticity. J Mech Phys Solids 59:344

29. Zhang HW, Zang S, Bi JY, Schrefler BA (2007) Thermo-mechanical analysis of periodic multiphase materials by a multi-scale asymptotic homogenization approach. Int J Numer Methods Eng 69:87

30. Temizer I (2012) On the asymptotic expansion treatment of two-scale finite thermoelasticity. Int J Eng Sci 53:74

31. Wu T, Temizer I, Wriggers P (2013) Computational thermal homogenization of concrete. Cem Concr Compos 35:59

32. Wu T, Temizer I, Wriggers P (2014) Multiscale hydro–thermo–chemo-mechanical coupling: application to alkali-silica reaction. Comput Mater Sci 84:381

33. Fish J, Yu Q (2001) Two-scale damage modeling of brittle composites. Compos Sci Technol 61:2215

34. Wriggers P, Moftah SO (2006) Mesoscale models for concrete: homogenisation and damage behaviour. Finite Elem Anal Des 42:623

35. Matouš K, Kulkarni MG, Geubelle PH (2008) Multiscale cohesive failure modeling of heterogeneous adhesives. J Mech Phys Solids 56:1511

36. Hirschberger CB, Ricker S, Steinmann P, Sukumar N (2009) Computational multiscale modelling of heterogeneous material layers. Eng Fract Mech 76:793

37. Holl M, Loehnert S, Wriggers P (2013) An adaptive multiscale method for crack propagation and crack coalescence. Int J Numer Methods Eng 93:23

38. Hill R (1972) On constitutive macro-variables for heterogeneous solids at finite strain. Proc R Soc Lond A 326:131

39. Waurick M (2013) Homogenization of a class of linear partial differential equations. Asymptot Anal 82:271

40. Popa C, Fleischhauer R, Schneider K, Kaliske M (2014) Formulation and implementation of a constitutive model for semicrystalline polymers. Int J Plast 61:128

41. Rieger S (2004) Temperaturabhängige Beschreibung visko-elasto-plastischer Deformationen kurzglasfaserverstärkter Thermoplaste: Modellbildung, Numerik und Experimente. PhD Thesis, Universität Stuttgart

42. Fleischhauer R, Qinami A, Hickmann R, Diestel O, Götze T, Cherif C, Heinrich G, Kaliske M (2015) A thermomechanical interface description and its application to yarn pullout tests. Int J Solids Struct 69–70:531

43. Božić M, Fleischhauer R, Kaliske M (2015) Thermomechanical modeling of epoxy/glass fiber systems including interphasial properties. Eng Comput 33:1259

44. Miehe C (1988) Zur Behandlung thermomechanischer Prozesse. PhD Thesis, Universität Hannover

45. Tømmernes V (2014) Implementation of the Arruda–Boyce material model for polymers in Abaqus. Master's Thesis, Norwegian University of Science and Technology